



Article

# Numerical Study of the Ultra-High-Speed Aerodynamically Alleviated Marine Vehicle Motion Stability in Winds and Waves

Yani Song , Xiaoxu Du \* and Yuli Hu

School of Marine Science and Technology, Northwestern Polytechnical University, No. 127, Youyi Road (West), Xi'an 710072, China

\* Correspondence: nwpudu@163.com

**Abstract:** The ultra-high-speed aerodynamically alleviated marine vehicle (AAMV) is a high-performance vessel that combines a hydrodynamic configuration and an aerodynamic wing to reduce wave-making resistance during the high-speed planing phase. The forces of the AAMV exhibit strong nonlinear and water–air coupling characteristics, resulting in particularly complex motion characteristics. This paper presents a longitudinal and lateral stability model of the AAMV, which considers the effects of aerodynamic alleviation. Additionally, a numerical model of wind and wave turbulence forces is established, which considers viscous correction based on the potential theory. Finally, the effect of wind and wave turbulence forces on the motion stability of the AAMV under regular and irregular waves is analyzed by numerical solution. The simulation results demonstrate the influence of these disturbance forces on the stability of the AAMV under different sea states. The motion parameters of the AAMV exhibit a pronounced response to changes in sea state level. The aerodynamically alleviated effect is enhanced as speed increases, and the influence of winds and waves on the AAMV is greatly weakened, reducing the possibility of instability. During the cruising phase under class V sea state, the pitch, roll, and heave response are  $0.210^\circ$ ,  $0.0229^\circ$ , and 0.0734 m, respectively. This effect can effectively improve the motion stability of the AAMV in winds and waves.

**Keywords:** aerodynamically alleviated marine vehicle; motion stability; potential theory; winds and waves



**Citation:** Song, Y.; Du, X.; Hu, Y. Numerical Study of the Ultra-High-Speed Aerodynamically Alleviated Marine Vehicle Motion Stability in Winds and Waves. *J. Mar. Sci. Eng.* **2024**, *12*, 1229. <https://doi.org/10.3390/jmse12071229>

Academic Editor: Kostas Belibassakis

Received: 12 June 2024

Revised: 18 July 2024

Accepted: 18 July 2024

Published: 21 July 2024



**Copyright:** © 2024 by the authors. Licensee MDPI, Basel, Switzerland. This article is an open access article distributed under the terms and conditions of the Creative Commons Attribution (CC BY) license (<https://creativecommons.org/licenses/by/4.0/>).

## 1. Introduction

In recent years, the demand for various high-speed marine vehicles has been increasing due to the transformation and upgrading of the marine economy and the increasingly complex maritime security situation. The shape of traditional high-speed marine vehicles does not meet the requirements for high speed and stability when sailing in winds and waves [1]. The ultra-high-speed aerodynamically alleviated marine vehicle (AAMV) is a new type of ship that combines hull and wing to create a high-performance vessel with low resistance and high lift. The hull of the AAMV adopts a deep-V shape, which increases the waterline coefficient and improves the stability of the AAMV in winds and waves. The aerodynamic structure utilizes a low aspect ratio wing to provide significant aerodynamic lift, raising the hull when sailing at high speeds by utilizing the ground effect. This reduces the wave resistance and minimizes the impact of waves.

According to the motion state, the AAMV can typically be categorized into three phases: low-speed drainage, medium-speed transition, and high-speed planing. The three phases of the AAMV motion are classified based on the Froude number  $Fr_B$ . Figure 1 illustrates the transition of the AAMV from the low-speed drainage phase to the high-speed planing phase. Throughout this process, the AAMV experiences both aerodynamic and hydrodynamic forces, which exhibit strong nonlinear and water–air coupling characteristics. The stability of the AAMV differs from that of traditional high-speed boats, making it more complex.

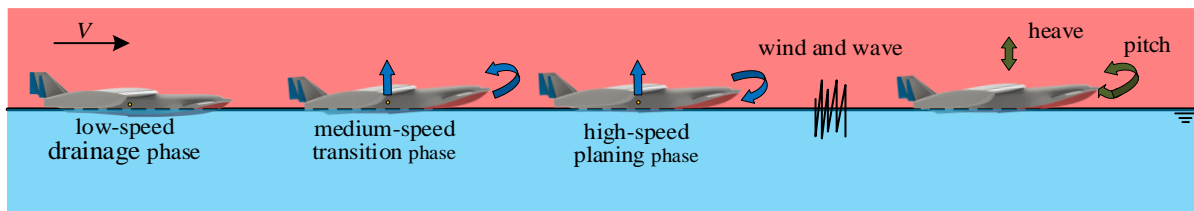


**Figure 1.** The motion process of the AAMV.

During the service life of the AAMV, the most common navigation condition is the sea environment under the combined effect of winds and waves. To ensure safe navigation of the AAMV under these conditions, it is essential to conduct comprehensive research and analysis on its stability. This is an important index for measuring the overall performance of the AAMV. Generally speaking, when exposed to wind and wave turbulence, the AAMV will experience pitch, roll, and yaw. If these motions become too extreme, the AAMV may become dangerously unstable and even capsize. Therefore, stability is crucial for the AAMV to operate safely in windy and wavy conditions.

Tests are a common and effective method for investigating vehicle performance. Two common types of tests are wind tunnel tests and towing tank tests. Wind tunnel tests are used to obtain the aerodynamic coefficients of the vehicle and determine its stability based on relevant stability criteria, such as Lyapunov stability theory [2]. To simulate the ground effects of vehicles operating in ground effect zones, such as the AAMV and ground-effect vehicles, scholars in the early days used the fixed-floor method in a laboratory environment [3,4]. With the progress of testing technology, moving floors, wave floors, and other devices have been created. Therefore, wind tunnel tests have also been gradually applied to the experimental study of the influence of waves on the AAMV [5]. For the AAMV, the towing tank test is the most intuitive and effective way to explore its motion stability due to its characteristic of always sailing on the water surface. During the test, parameters such as the position of the center of gravity and the mass of the model can be adjusted in order to investigate the impact of relevant design parameters on the stability of the vehicle [6]. In addition, the towing tank can simulate motion characteristics in winds and waves using the wave maker and draught fan, making it a widely used test.

Another common method for carrying out stability analysis is by solving the motion equations. The accurate establishment of a six-degree-of-freedom (6-DOF) mathematical model for high-speed vessels presents a significant challenge due to their nonlinear and multi-degree-of-freedom motion coupling characteristics. In response to this difficulty, researchers at home and abroad have typically opted to simplify the model to a certain extent. The simplified models proposed so far are based on the simplified one-degree-of-freedom model proposed by Fossen in 1994 [7]. The model is based on the theorem of momentum. It is assumed that the mass distribution of the model is uniform, that gravity and buoyancy act on the vertical axis of the model, and that the coupling between the degrees of freedom of the system is not considered. Later, Matveev used a three-degree-of-freedom kinematic model considering coupled surge–pitch–heave motion to simulate the maneuvering of a hydrofoil craft [8]. Sahin et al. developed the two-degree-of-freedom motion (pitch and heave) equations of the planing hull with an interceptor and designed a closed-loop control system using a linear quadratic regulator (LQR) controller for adjusting the height of the interceptor so as to obtain the optimal pitch angle at the minimum drag. In order to obtain a linear state-space model for the LQR design, the system is linearized around the equilibrium point of motion, and the hydrodynamic coefficients are all obtained using the relevant empirical formulas [9]. In the motion process of the AAMV, it is important to consider both aerodynamic and hydrodynamic forces. Therefore, when modeling the motion equations, the aerodynamic term should be added to the conventional hydrodynamic boat motion equation to obtain the motion equation of the AAMV. Then the state-space equation is derived using the small perturbation assumption, and the Routh–Hurwitz stability criterion is used to assess the motion stability [10,11]. Currently,

scholars focus on the longitudinal stability of the AAMV and pay less attention to its lateral stability [12,13]. The hydrodynamic and aerodynamic coefficients in the motion equations are typically obtained through theoretical analysis or empirical formulas [14,15], or they are directly borrowed from the coefficients of other similar shapes, which may affect the forecasting precision.

Computational fluid dynamics (CFD) technology is now being used to calculate the motion stability of the AAMV in calm water and waves [16]. This technology is favored for its lower cost and higher accuracy and is widely used in the instability simulation of high-speed vessels in waves [17–19]. In addition, accurate hydrodynamic coefficients serve as the foundation for analyzing the stability of marine vehicles. With the advent of overset mesh technology, the precision of hydrodynamic coefficients based on the CFD has been significantly improved [20]. CFD has gradually emerged as a primary approach for investigating the hydrodynamic performance of high-speed vessels [21–24]. An important hydrodynamic structure of the AAMV is the step on the planing surface, which can greatly reduce resistance and enable the AAMV to exhibit excellent navigation performance. In recent years, the hydrodynamic performance of planing hulls with one or two steps has been extensively studied [25]. Trimulyono et al. conducted a simulation of the influence of a double steps arrangement on the motion performance (drag, pitch, and heave) of a planing hull based on the CFD method with an overset mesh method. This analysis established the relationship between the position of the double steps and the drag, pitch, and heave after dimensionless processing [26]. In addition to the step, the interceptor is also an important structure for reducing drag and improving motion performance. Samuel et al. established a hydrodynamic numerical model of a planing hull with an interceptor by using the DFBI model in the commercial CFD software, STAR CCM+. The influence of the position and height of the interceptor on the motion performance of the planing hull was then analyzed [27]. These works are of great significance in guiding the optimal design of the planing hulls.

The AAMV is capable of generating a six-degree-of-freedom motion in response to wind and wave forces, as illustrated in Figure 2. For the force calculation of the AAMV in winds and waves, there are two common types of methods: the potential flow theory method and the RANS method. The potential flow theory, which is one of the earliest developments of wave theory, considers the ideal fluid flow around an object without taking viscosity into account. It is a mature method that accurately predicts the disturbance force of regular and irregular waves at different incidence angles and frequencies. Many scholars have used the potential flow theory to calculate the force of marine vehicles [28,29]. In addition, the potential flow theory can also be used to carry out direct simulations of the motion stability of high-speed ships in waves, including heading stability and steering stability [30]. The RANS method considers viscous effects and provides more accurate predictions for high-speed marine vehicles [31]. The overset grid technology has significantly improved the accuracy of predicting the motion of these vehicles in waves, which agrees well with experimental results [32].

Currently, there are relatively few studies on the stability of the AAMV in the open literature, as it is still in a rapid development stage. Previous studies have mainly focused on the longitudinal stability of AAMVs in the ground effect region after takeoff, with comparatively less attention paid to lateral stability [12,13]. Additionally, there is a paucity of research investigating the phenomenon of motion stability in waves. In contrast, this paper considers the stability of an AAMV on the water surface, where the coupled hydrodynamic and aerodynamic forces act. It is therefore of great theoretical and practical significance to study the longitudinal and lateral stability of the AAMV in waves. This approach allows for a multiphase flow stability analysis, which addresses some of the gaps in the existing research. This paper is organized as follows: Section 2 provides a description of the AAMV. In Section 3, a 6-DOF motion model considering aerodynamic alleviation is established as the basis for the stability analysis in wind and waves. In this section, a numerical model of the wind and wave turbulence forces of the AAMV is also established based on the

panel method. This model is used to simulate the wind and wave turbulence forces of the AAMV under different sea conditions. These simulations can be combined with the 6-DOF equations to describe the 6-DOF motion of the AAMV in wind and waves. In Section 4, the mathematical model is simplified by decoupling the longitudinal and lateral motions, which are assumed to be weakly coupled. The mathematical model is then linearized based on the small-perturbation theory, which allows the longitudinal and lateral stability models of the AAMV in wind and waves to be obtained. Section 5 discusses the motion stability of the AAMV in wind and waves, and Section 6 presents the conclusion of this paper.

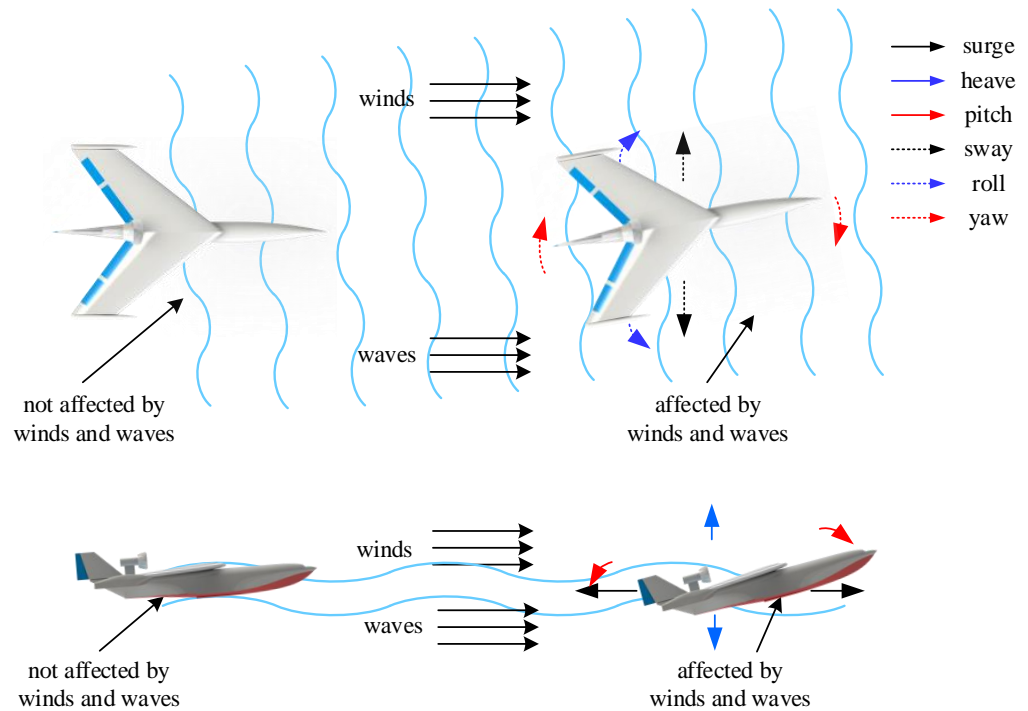


Figure 2. The motion of the AAMV under the influence of winds and waves.

## 2. The Configuration of the AAMV

Figure 3 shows the basic configuration of the AAMV, which consists of a deep V-shaped hull with a sharpened bottom and aerodynamic wing. Floats are added at the ends of the wing to improve lateral stability, while a transverse step is installed on the planing surface to reduce hydrodynamic resistance and increase longitudinal stability. The AAMV’s propulsion system utilizes an aero-engine positioned above the hull to generate thrust parallel to its longitudinal axis. Elevation and roll control are achieved through flaps and ailerons located at the trailing edge of the wing, while heading control is maintained by the rudder at the trailing edge of the vertical fin. Figure 4 shows the definitions, and Table 1 displays the values of the main parameters of the AAMV.

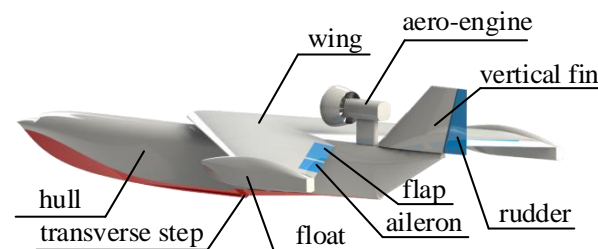


Figure 3. Overall shape of the AAMV.

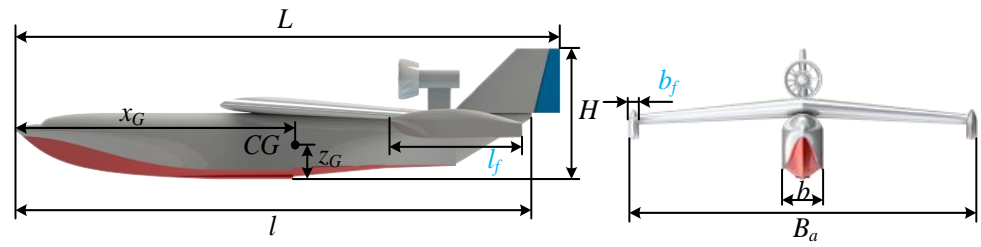


Figure 4. Definitions of the main parameters.

Table 1. Values of the main parameters.

Main Parameters	Notation	Unit	Value
total length	$L$	m	92.50
total width	$B_a$	m	56.40
total height	$H$	m	21.30
mass	$m$	t	500.00
longitudinal center of gravity	$x_G$	m	36.88
vertical center of gravity	$z_G$	m	7.28
hull	length	$l$	89.00
	width	$b$	7.00
float	length	$l_f$	38.00
	width	$b_f$	0.90

### 3. Motion Model

#### 3.1. Coordinate System and Parameter Definition

To study the 6-DOF motion mathematical model of the AAMV, three right-handed rectangular coordinate systems are required: a ground coordinate system  $O_0-x_0y_0z_0$  fixed in space, a body coordinate system  $G-xyz$  fixed to the AAMV and following its motion, and a velocity coordinate system  $G-x_1y_1z_1$  to characterize its velocity. Figure 5 displays the established coordinate systems.

In order to describe the spatial state of the AAMV, it is necessary to define the motion parameters of the vehicle. The motion state of the AAMV can then be determined by the defined motion parameters. This paper studies the motion stability of the AAMV in winds and waves, which requires consideration of the six degrees of freedom: surge, sway, heave, roll, pitch, and yaw. Figure 5 and Table 2 display their corresponding motion forms and parameters. The transformation matrix between different coordinate systems, as well as the definitions of angle of attack  $\alpha$  and sideslip angle  $\beta$ , are presented in Reference [33].

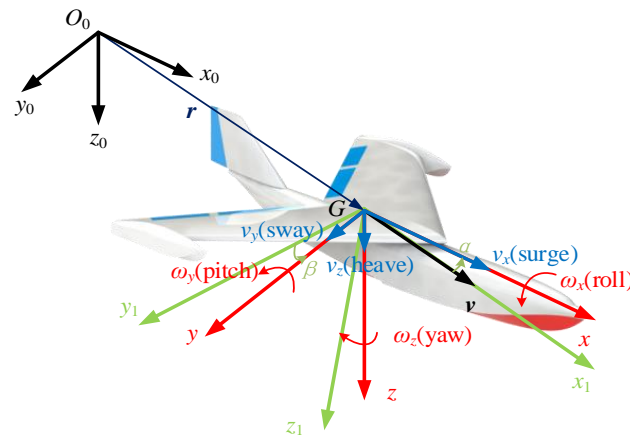


Figure 5. Coordinate system of the AAMV.

Table 2. Motion parameters of the AAMV.

Axis	Ground Coordinate System			Body Coordinate System		
	Description	Translation	Linear Velocity	Description	Rotation	Angular Velocity
<i>x</i>	surge	$x_0$	$v_x$	roll	$\phi$	$\omega_x$
<i>y</i>	sway	$y_0$	$v_y$	pitch	$\theta$	$\omega_y$
<i>z</i>	heave	$z_0$	$v_z$	yaw	$\psi$	$\omega_z$

### 3.2. Kinematic Model

The 6-DOF motion equations of the AAMV include two parts: the kinematic model and the kinetic model. The establishment of kinematic equations is employed to delineate the interrelationship between displacement and velocity, angle and angular velocity, and other related variables. By utilizing the transformation relationship between the coordinate systems mentioned above, we can derive the 6-DOF kinematic model of the AAMV (Equations (1) and (2)). The spatial position and attitude of the AAMV at any given moment can be obtained through integration.

$$\begin{bmatrix} \dot{x}_0 \\ \dot{y}_0 \\ \dot{z}_0 \end{bmatrix} = C_g^b \begin{bmatrix} v_x \\ v_y \\ v_z \end{bmatrix} \tag{1}$$

$$\begin{bmatrix} \dot{\phi} \\ \dot{\theta} \\ \dot{\psi} \end{bmatrix} = \omega_g^b \begin{bmatrix} \omega_x \\ \omega_y \\ \omega_z \end{bmatrix} \tag{2}$$

where  $C_g^b$  and  $\omega_g^b$  are the transformation matrices from the body coordinate system to the ground coordinate system.

### 3.3. Kinetic Model

The kinetic equations of the AAMV are established to describe the relationship between force/moment and motion. The kinetic model of the AAMV differs from that of conventional high-speed marine vehicles or airplanes, which are subject to both hydrodynamic and aerodynamic forces. In the case of the AAMV, aerodynamic forces should be considered based on the motion model of a conventional high-speed marine vehicle, while the additional mass should be taken into account based on the motion model of an airplane. Assuming that the AAMV is a rigid body with constant mass and shape and that its motion model adheres to the basic principles of Newton’s mechanics, the kinetic model of the AAMV in the body coordinate system can be expressed as Equation (3), following the theorem of momentum.

$$M \begin{bmatrix} \dot{v}_x \\ \dot{v}_y \\ \dot{v}_z \\ \dot{\omega}_x \\ \dot{\omega}_y \\ \dot{\omega}_z \end{bmatrix} + A_{V\Omega} \left\{ M \begin{bmatrix} v_x \\ v_y \\ v_z \\ \omega_x \\ \omega_y \\ \omega_z \end{bmatrix} \right\} = \begin{bmatrix} F_x \\ F_y \\ F_z \\ M_x \\ M_y \\ M_z \end{bmatrix} \tag{3}$$

where,

$$M = \begin{bmatrix} m & 0 & 0 & 0 & 0 & 0 \\ 0 & m & 0 & 0 & 0 & 0 \\ 0 & 0 & m & 0 & 0 & 0 \\ 0 & 0 & 0 & I_{xx} & 0 & 0 \\ 0 & 0 & 0 & 0 & I_{yy} & 0 \\ 0 & 0 & 0 & 0 & 0 & I_{zz} \end{bmatrix} \tag{4}$$

$$A_{V\Omega} = \begin{bmatrix} 0 & -\omega_z & \omega_y & 0 & 0 & 0 \\ \omega_z & 0 & -\omega_x & 0 & 0 & 0 \\ -\omega_y & \omega_x & 0 & 0 & 0 & 0 \\ 0 & -v_z & v_y & 0 & -\omega_z & \omega_y \\ v_z & 0 & -v_x & \omega_z & 0 & -\omega_x \\ -v_y & v_x & 0 & -\omega_y & \omega_x & 0 \end{bmatrix} \quad (5)$$

$m$  is the mass of the AAMV;  $I_{xx}, I_{yy}, I_{zz}$  are the rotational inertia of the AAMV;  $F_x, F_y, F_z, M_x, M_y, M_z$  are the forces and moments in the body coordinate system.

### 3.4. Kinetic Analysis

This section is devoted to the analysis of the forces acting on the AAMV as it moves in waves. The forces  $\mathbf{F}$  acting on the AAMV can be classified into four main types: gravity  $\mathbf{F}_g$ , fluid dynamical force  $\mathbf{F}_f$ , operating force  $\mathbf{F}_o$ , and disturbance force  $\mathbf{F}_d$ . The fluid dynamic forces acting on the AAMV can be categorized as hydrodynamic force  $\mathbf{F}_h$  and aerodynamic force  $\mathbf{F}_a$ , depending on the fluid medium. The operating forces mainly consist of the aerodynamic thrust  $\mathbf{F}_t$  generated by the engine and the rudder force  $\mathbf{F}_r$  generated by the rudder and flap. The disturbance forces mainly consist of the winds, waves, and ocean currents. Equation (6) and Figure 6 depict the forces of the AAMV.

$$\mathbf{F} = \mathbf{F}_g + \mathbf{F}_h + \mathbf{F}_a + \mathbf{F}_o + \mathbf{F}_d \quad (6)$$

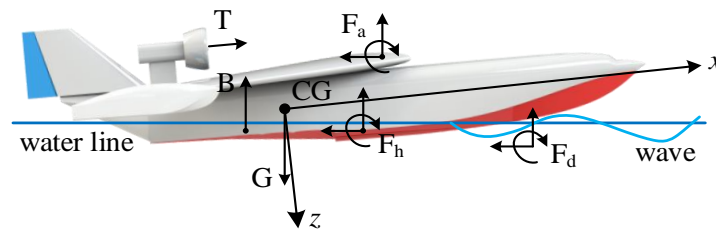


**Figure 6.** Force analysis of the AAMV.

#### 3.4.1. Gravitational Force

Its components on each axis in the body coordinate system are displayed in Equation (7).

$$\mathbf{F}_g = \begin{bmatrix} X_g \\ Y_g \\ Z_g \end{bmatrix} = C_b^0 \begin{bmatrix} 0 \\ 0 \\ G \end{bmatrix} = \begin{bmatrix} -G \sin \theta \\ G \cos \theta \sin \phi \\ G \cos \theta \cos \phi \end{bmatrix} \quad (7)$$

#### 3.4.2. Hydrodynamic Force

According to the principle of force, hydrodynamic forces on the AAMV are divided into buoyancy  $\mathbf{F}_b$ , added mass  $\mathbf{F}_i$ , and viscous forces  $\mathbf{F}_v$ , as shown in Equation (8).

$$\mathbf{F}_h = \mathbf{F}_b + \mathbf{F}_i + \mathbf{F}_v \quad (8)$$

##### (1) Buoyancy

Equations (9) and (10) display the force and moment components of buoyancy  $B$  on each axis in the body coordinate system.

$$\mathbf{F}_B = \begin{bmatrix} X_b \\ Y_b \\ Z_b \end{bmatrix} = C_b^0 \begin{bmatrix} 0 \\ 0 \\ -B \end{bmatrix} = \begin{bmatrix} B \sin \theta \\ -B \cos \theta \sin \phi \\ -B \cos \theta \cos \phi \end{bmatrix} \quad (9)$$

$$\mathbf{M}_B = \begin{bmatrix} M_{Bx} \\ M_{By} \\ M_{Bz} \end{bmatrix} = \begin{bmatrix} 0 & -z_c & y_c \\ z_c & 0 & x_c \\ -y_c & x_c & 0 \end{bmatrix} \begin{bmatrix} X_b \\ Y_b \\ Z_b \end{bmatrix} = \begin{bmatrix} B \cos \theta (z_c \sin \phi - y_c \cos \phi) \\ -B (z_c \sin \theta + x_c \cos \theta \cos \phi) \\ B (y_c \sin \theta - x_c \cos \theta \sin \phi) \end{bmatrix} \quad (10)$$

Thus, Equation (11) displays the buoyancy  $F_b$  in the body coordinate system.

$$F_b = \begin{bmatrix} F_B \\ M_B \end{bmatrix} \tag{11}$$

(2) Added mass

The expression of the added mass in the body coordinate system in ideal fluid is shown in Equation (12), since the AAMV is symmetric about the  $xGz$  plane.

$$F_I = \begin{bmatrix} X_I \\ Y_I \\ Z_I \\ M_{Ix} \\ M_{Iy} \\ M_{Iz} \end{bmatrix} = \lambda \begin{bmatrix} \dot{v}_x \\ \dot{v}_y \\ \dot{v}_z \\ \dot{\omega}_x \\ \dot{\omega}_y \\ \dot{\omega}_z \end{bmatrix} + A_{V\Omega} \left\{ \lambda \begin{bmatrix} v_x \\ v_y \\ v_z \\ \omega_x \\ \omega_y \\ \omega_z \end{bmatrix} \right\} \tag{12}$$

where the additional mass matrix  $\lambda$  can be expressed as:

$$\lambda = \begin{bmatrix} \lambda_{11} & 0 & 0 & 0 & 0 & 0 \\ 0 & \lambda_{22} & 0 & \lambda_{24} & 0 & \lambda_{26} \\ 0 & 0 & \lambda_{33} & 0 & \lambda_{35} & 0 \\ 0 & \lambda_{42} & 0 & \lambda_{44} & 0 & \lambda_{46} \\ 0 & 0 & \lambda_{53} & 0 & \lambda_{55} & 0 \\ 0 & \lambda_{62} & 0 & \lambda_{64} & 0 & \lambda_{66} \end{bmatrix} \tag{13}$$

where  $\lambda_{ij}$  is the added inertia and mass of the AAMV, which can be calculated by CFD or an empirical formula.

(3) Viscous forces

The viscous forces experienced by the AAMV during navigation can be classified into positional hydrodynamic forces, which are related to the angle of attack  $\alpha$  and sideslip angle  $\beta$ , and damping hydrodynamic forces, which are related to the angular velocity  $\omega_x, \omega_y, \omega_z$  (as shown in Equation (14)).

$$F_v = \begin{bmatrix} X_v \\ Y_v \\ Z_v \\ M_{xv} \\ M_{yv} \\ M_{zv} \end{bmatrix} = \frac{1}{2} \rho S_w V^2 \begin{bmatrix} C_x^\alpha \alpha \\ C_y^\beta \beta + C_y^{\omega_z} \omega_z \\ C_z^\alpha \alpha + C_z^{\omega_y} \omega_y \\ l m_x^{\omega_x} \omega_x \\ l m_y^\alpha \alpha + l m_y^{\omega_y} \omega_y \\ l m_z^\beta \beta + l m_z^{\omega_z} \omega_z \end{bmatrix} \tag{14}$$

where  $S_w$  is the wetted area of the AAMV;  $l$  is the length of the hull;  $C_i^\alpha, C_i^\beta, m_i^\alpha, m_i^\beta$  represent the viscous forces (moments) coefficient induced by the angle of attack  $\alpha$  and sideslip angle  $\beta$  on the  $i$ -axis;  $C_i^{\omega_j}, m_i^{\omega_j}$  represent the viscous forces (moments) coefficient on the  $i$ -axis induced by the angular velocity around the  $j$ -axis ( $\omega_j$ ).

3.4.3. Aerodynamic Force

The aerodynamic force generated by the wing at high speeds cannot be ignored. In this paper, the design speed of the AAMV is 100 kn, and air is considered an incompressible fluid medium, so the effect of aeroelasticity on the AAMV is not a concern. Equation (15) shows the expression for the aerodynamic force of the AAMV.



$$\mathbf{F}_a = \begin{bmatrix} X_a \\ Y_a \\ Z_a \\ M_{xa} \\ M_{ya} \\ M_{za} \end{bmatrix} = \frac{1}{2} \rho_a S_a V^2 \begin{bmatrix} C_{xa}^\alpha \alpha \\ C_{ya}^{\omega_z} \omega_z + C_{ya}^\beta \beta \\ C_{za}^{\omega_y} \omega_y + C_{za}^\alpha \alpha \\ B_a m_{xa}^{\omega_x} \omega_x \\ l_a (m_{ya}^{\omega_y} \omega_y + m_{ya}^\alpha \alpha) \\ B_a (m_{za}^{\omega_z} \omega_z + m_{za}^\beta \beta) \end{bmatrix} \tag{15}$$

where  $\rho_a$  represents the density of air;  $S_a$  is the area of the wing;  $B_a$  is the length of the wing span;  $l_a$  is the chord length of the wing;  $C_{ia}^\alpha$ ,  $C_{ia}^\beta$ ,  $m_{ia}^\alpha$ ,  $m_{ia}^\beta$  represent the aerodynamic forces (moments) coefficient induced by the angle of attack  $\alpha$  and sideslip angle  $\beta$  on the  $i$ -axis;  $C_{ia}^{\omega_j}$ ,  $m_{ia}^{\omega_j}$  represent the aerodynamic forces (moments) coefficient on the  $i$ -axis induced by the angular velocity around the  $j$ -axis ( $\omega_j$ ).

### 3.4.4. Operating Force

The operating forces of the AAMV consist mainly of thrust and rudder forces. As dictated by the layout of the AAMV, the thrust  $T$  generated by the aeroengine is parallel to the  $Gx$ -axis of the body coordinate system, and the operating force expression is shown in Equation (16).

$$\mathbf{F}_c = \begin{bmatrix} X_c \\ Y_c \\ Z_c \\ M_{xc} \\ M_{yc} \\ M_{zc} \end{bmatrix} = \frac{1}{2} \rho S V^2 \begin{bmatrix} \frac{2T}{\rho S V^2} \\ C_y^{\delta_r} \delta_r \\ C_z^{\delta_f} \delta_f \\ l m_x^{\delta_a} \delta_a \\ L m_y^{\delta_f} \delta_f \\ L m_z^{\delta_r} \delta_r \end{bmatrix} \tag{16}$$

where  $T$  is the thrust force;  $\delta_f$ ,  $\delta_r$ , and  $\delta_a$  are the angles of flap, rudder, and aileron, respectively;  $C_y^{\delta_r}$ ,  $C_z^{\delta_f}$ ,  $m_x^{\delta_a}$ ,  $m_y^{\delta_f}$ ,  $m_z^{\delta_r}$  are the rudder forces (moments) on different axes, respectively.

### 3.4.5. Wind and Wave Disturbance Force

Disturbances during navigation are mainly caused by wind and waves. The wind impacts the upper aerodynamic structure of the AAMV, while the wave acts on the lower hydrodynamic structure. The two forces interact with each other, leading to complex wind and wave disturbances, as shown in Figure 7. In order to analyze the stability of the AAMV during navigation, it is necessary to analyze the effect of wind and waves on it.

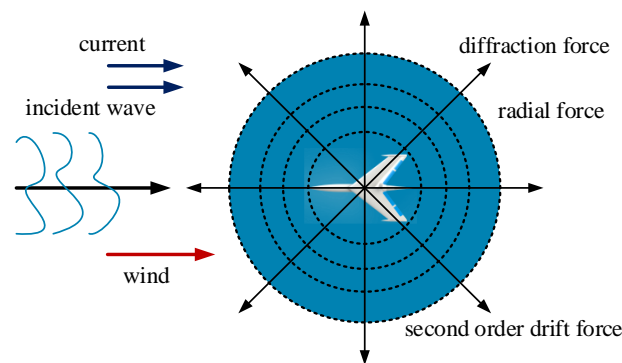


Figure 7. The forces of the AAMV in wind and waves.

In this section, a numerical model for the sea loads of the AAMV is established in the hydrodynamic analysis software ANSYS AQWA based on the regular wave theory and the three-dimensional potential theory. The model is then used to simulate the motion of the AAMV in waves based on the panel method. Finally, the sea loads suffered by the AAMV under different sea conditions and different wave incidence angles are obtained through frequency domain and time domain analysis.

#### (1) Force analysis for the problem of the AAMV motion in regular waves

Higher-order Stokes waves with high crests and flat troughs are similar to natural wave propagation. Therefore, this paper uses the fifth-order wave to describe the wave surface equation and velocity components of the fifth-order Stokes wave. The wind speed profile describes the variation in wind speed with altitude. The currents are treated as uniform currents, and the force of the currents on the AAMV is described using relative velocities. That is, when the AAMV moves in the current, it is equivalent to superimposing another current flow field on the original flow field of the AAMV.

Potential flow theory is used to solve the wind and wave forces on the AAMV. In this theoretical framework, the fluid is assumed to be an inviscid, irrotational, incompressible ideal fluid. In the case of regular waves, the first-order velocity potential of the AAMV can be decomposed into the velocity potential of the incident wave, the velocity potential of the diffraction wave, and the velocity potential of the radiation wave, which can be solved separately [34,35].

The panel method is used to solve the wind and wave forces acting on the AAMV. The AAMV surface is discretized into multiple panels. The original surface is substituted by these components, which are arranged into control points on the wetted surface, such as source–sinks. Consequently, the first-order wave forces acting on the AAMV can be obtained. Furthermore, despite being smaller than the first-order force, the second-order drift force is the primary cause of significant motion for surface vehicles in the horizontal plane. This occurs, in particular, when the frequency of the drift force closely matches the natural frequency of the vehicle, leading to resonance [36].

#### (2) Numerical model and viscosity correction

Three-dimensional potential theory neglects the viscous effect of the fluid. In the actual navigation process, viscous damping plays a pivotal role in ensuring safe navigation for the AAMV. However, the calculation results of the three-dimensional potential theory are less accurate due to the inclusion of viscous damping. Furthermore, when the AAMV resonates with waves, the calculation using three-dimensional potential theory will produce significant errors. It is thus imperative to modify the viscous damping of the numerical model based on potential theory. To illustrate, consider the example of pitch damping:

$$D_{\mu 2} = 2\mu_y \sqrt{(I_{yy} + \Delta I_{yy})K_{pitch}} \quad (17)$$

where  $I_{yy}$  is the pitch moment of inertia of the AAMV;  $\Delta I_{yy}$  is the additional pitch moment of inertia;  $K_{pitch}$  is the pitch stiffness;  $\mu_y$  is the pitch damping correction coefficient, which is determined from the CFD results.

The aforementioned damping coefficients are added to the numerical model as additional damping, and the numerical model considering viscous correction can be obtained. Subsequently, the model is meshed, with the minimum mesh size set to 0.8% of the total length of the AAMV and the minimum frequency corresponding to the mesh being 0.025 Hz. These values ensure that the number of meshes does not exceed the limit and that the computational requirements are met [37]. The computational domain is a 1000-m-long, 1000-m-wide, and 100-m-deep area of water, and the draft of the AAMV is 3.2 m. Figure 8 illustrates the computational domain and mesh arrangement.

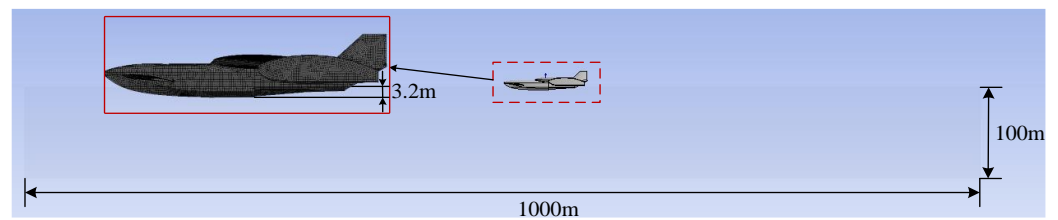


Figure 8. Computational domain and mesh arrangement.

The simulation of wind and wave disturbance forces acting on the AAMV under different sea conditions is based on factors such as wind speed, significant wave height, wavelength, and wave frequency. To improve computational efficiency, the incidence angle is set to  $0^\circ\sim 180^\circ$ , considering the AAMV is symmetric with respect to the  $xGz$  plane in the body coordinate system. Table 3 and Figure 9 show the specific simulation condition settings.

Table 3. Simulation condition settings.

Sea State	Wind Speed/(m/s)	Significant Wave Height/m	Wavelength/m	Wave Frequency/Hz
Class II	4.37	0.366	6.10	0.505
Class III	6.95	0.884	15.85	0.313
Class IV	9.78	2.103	30.18	0.227
Class V	12.60	3.962	50.00	0.177

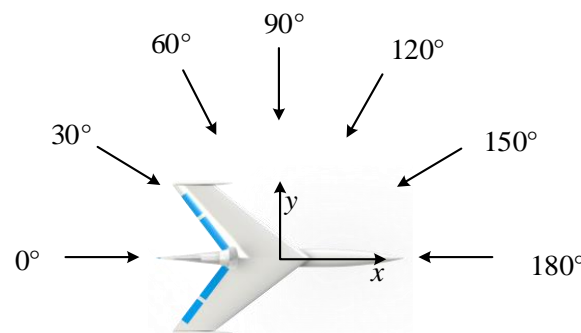


Figure 9. The incidence angle of the AAMV.

### (3) Verification and validation study

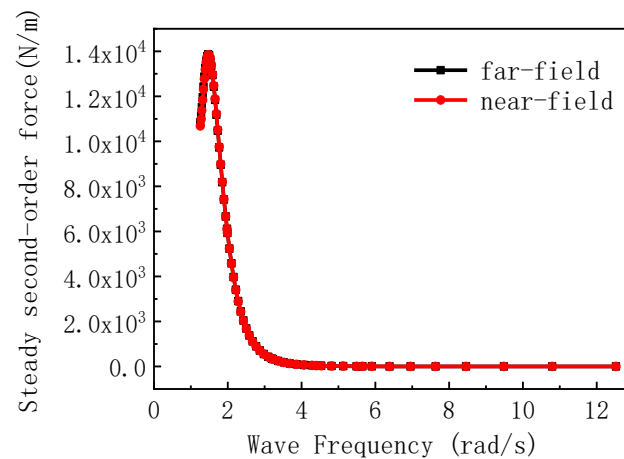
In accordance with the guidelines set forth by the ITTC [38], the convergence analysis is initially conducted. Verification is the process of evaluating the numerical uncertainty present in simulations, which is primarily attributable to grid uncertainty. The wave loads on the AAMV under the action of a regular wave at  $0^\circ$  incidence angle in a class IV sea state are calculated using three sets of grids. The results are presented in Table 4.

Table 4. Grid convergence study.

Grids	Grid Sizes	Grid Numbers	Surge Wave Loads $F_x/N$
coarse	1.1%L	21,494	13,257.4
medium	0.9%L	29,059	13,262.5
fine	0.8%L	38,345	13,277.3

The convergence ratio,  $R_G$ , is 0.34, which meets the requirement of  $0 < R_G < 1$ , indicating that monotonic convergence is achieved.

The AQWA offers two distinct methodologies for the solution of the sea loads on the AAMV: the near-field and the far-field [37]. The near-field method is based on the panel method, which can directly solve the six-degree-of-freedom wave forces of the AAMV. However, the accuracy of the computational results is primarily dependent on the mesh division of the panel method. The far-field method employs the momentum theorem for solution, yet it is limited to the calculation of three-degree-of-freedom wave forces in the horizontal plane. This approach offers high solution accuracy but a narrow application range. The near-field method (panel method) is typically employed to resolve the wave force of the AAMV. The accuracy of the near-field method and the quality of the mesh in the panel method are validated by comparing the results of the second-order wave force between the near-field and far-field methods. When the results of the two calculations converge and the error is not too large, it can be reasonably assumed that the accuracy of the near-field method is sufficient to meet the requirements of the panel method numerical model. The third set of grids in Table 4 is selected for comparison, and the results are presented in Figure 10. As illustrated in Figure 10, the results of the two methods are consistent, with an average error of 1.61%. It can thus be concluded that the panel method model is capable of meeting the requisite calculation accuracy standards.



**Figure 10.** Comparison of the results of steady second-order force between the near-field method and the far-field method.

To further verify the accuracy of the model, a CFD model based on the RANS method was used to simulate the wave loads on the AAMV under the action of a regular wave at a 0° incidence angle in a class IV sea state. This was verified with the numerical model established based on the potential theory presented in this paper. The numerical model, based on the RANS method, and its validation study are presented in Reference [16].

The time-domain curves of the wave force based on the potential theory and the RANS method are presented in Figure 11, and the comparison results of the amplitude calculated by the two models are provided in Table 5. The results demonstrate that the potential theory model, which incorporates a viscous correction, is generally consistent with those of the RANS method. The amplitude error is within 10%, indicating that the wave loads obtained by the potential theory method and the CFD model based on the RANS method are objective and consistent. Therefore, the numerical model established in this paper is reliable, which can provide a certain reference for the subsequent development of similar simulations.

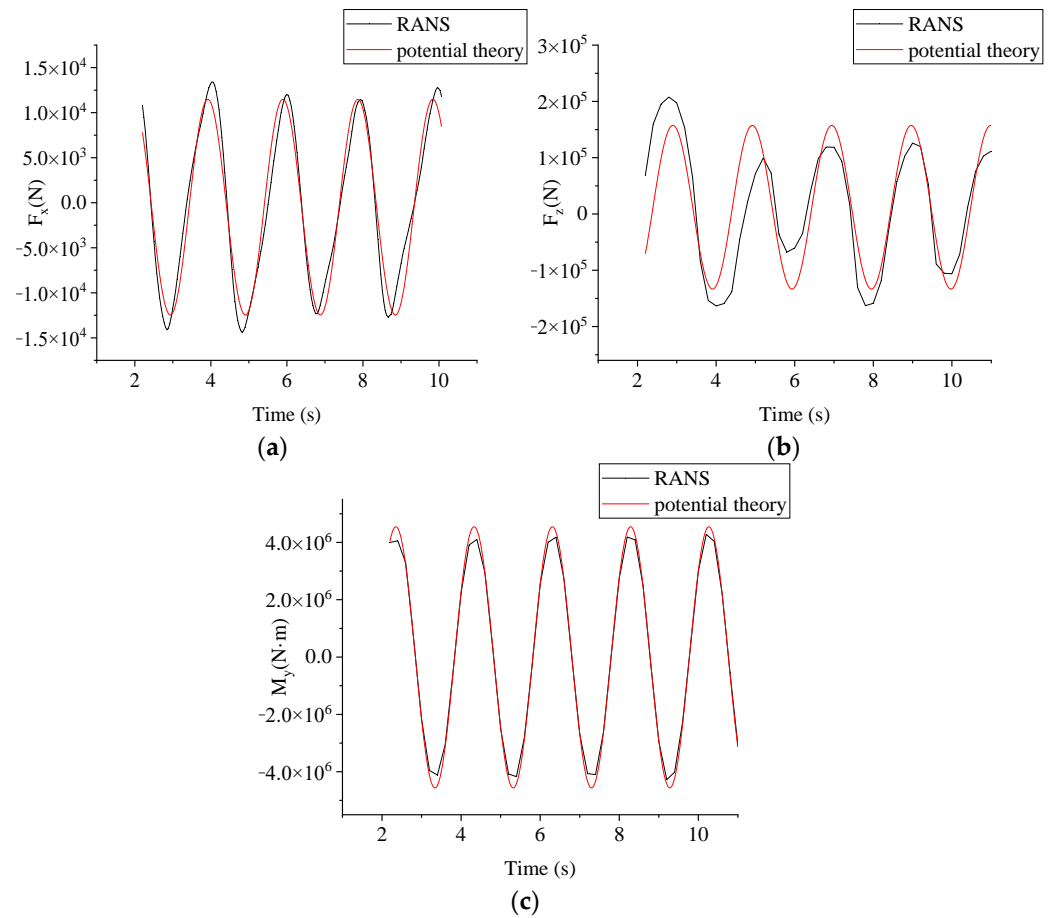


**Figure 11.** Comparison curve between the results obtained from the RANS method and the potential theory method. (a) surge force  $F_x$ ; (b) heave force  $F_z$ ; (c) pitch moment  $M_y$ .

**Table 5.** Comparison of amplitude obtained from the RANS method and the potential theory method.

Method	$F_x/N$	$F_z/N$	$M_y/N \cdot m$
RANS	13,967.7	136,892.1	4,251,607.9
Potential theory	13,277.3	150,088.3	4,468,080.5
Error	5.2%	8.7%	4.8%

#### (4) Numerical results

The results of the first-order force transfer function for different incidence angles are given in Figure 12. Due to the complex aerodynamic structure of the AAMV and its hydrodynamic configuration of the main hull and end plate pontoons, the coupling effect of the structure results in the appearance of multiple peaks of the first-order wave force amplitude at both medium and high frequencies. In general, the pitch response amplitude is the largest, while the amplitudes of sway and roll responses are smaller than those in other directions, indicating that the first-order force has the most significant influence on the pitch motion of the AAMV and has a minimal effect on the lateral motion.

The amplitude and variation in longitudinal wave forces remain consistent in both the longitudinal head-waves and following-waves, within a variance range of  $\pm 30^\circ$  of wave incidence angles. In this range, changes in incident angles have little effect on the first-order longitudinal forces. In transverse wave motion, the first-order transverse force peaks appear when the incident angle is  $90^\circ$ . In oblique waves, first-order force transfer functions have multiple peaks, and the first-order forces at high frequencies are generally smaller than those at low frequencies.

In the vertical direction, the amplitude of the first-order force decreases with the increase in frequency, indicating that the heave motion response of the AAMV grows progressively with higher sea states. Except for the vertical direction, the amplitude of the first-order force shows an increasing and then decreasing tendency as the frequency increases. The peak values of surge and pitch forces appear near the frequency of 0.12 Hz. The peak values of roll and sway forces appear near the frequency of 0.27 Hz. The peak value of the yaw force appears near the frequency of 0.20 Hz. In the navigational sea state of the AAMV, the wave frequencies range from 0.227 Hz to 0.505 Hz. Therefore, the AAMV operates in a relatively safe frequency range during navigation, resulting in much smaller actual wave forces than the peaks of first-order wave forces.

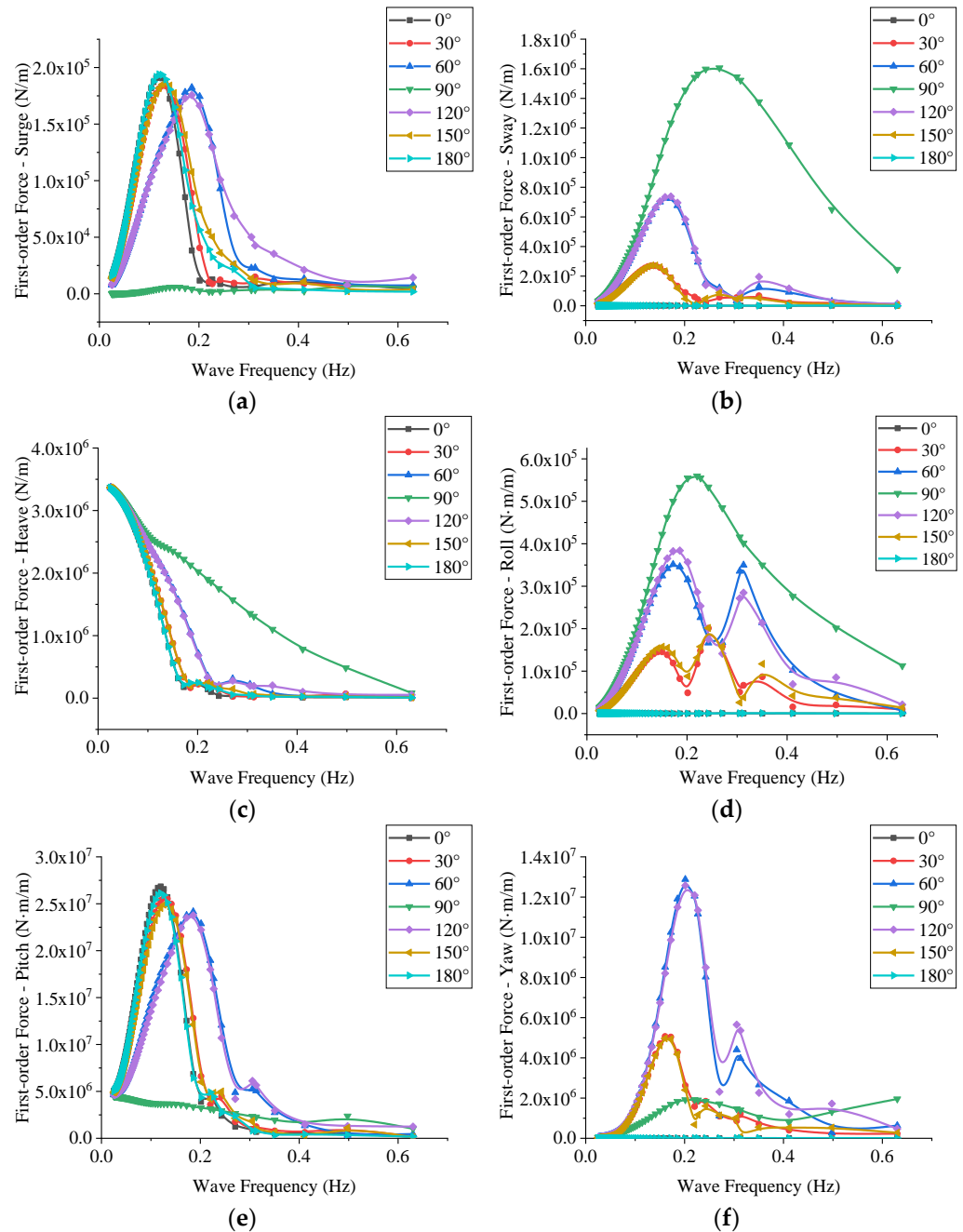
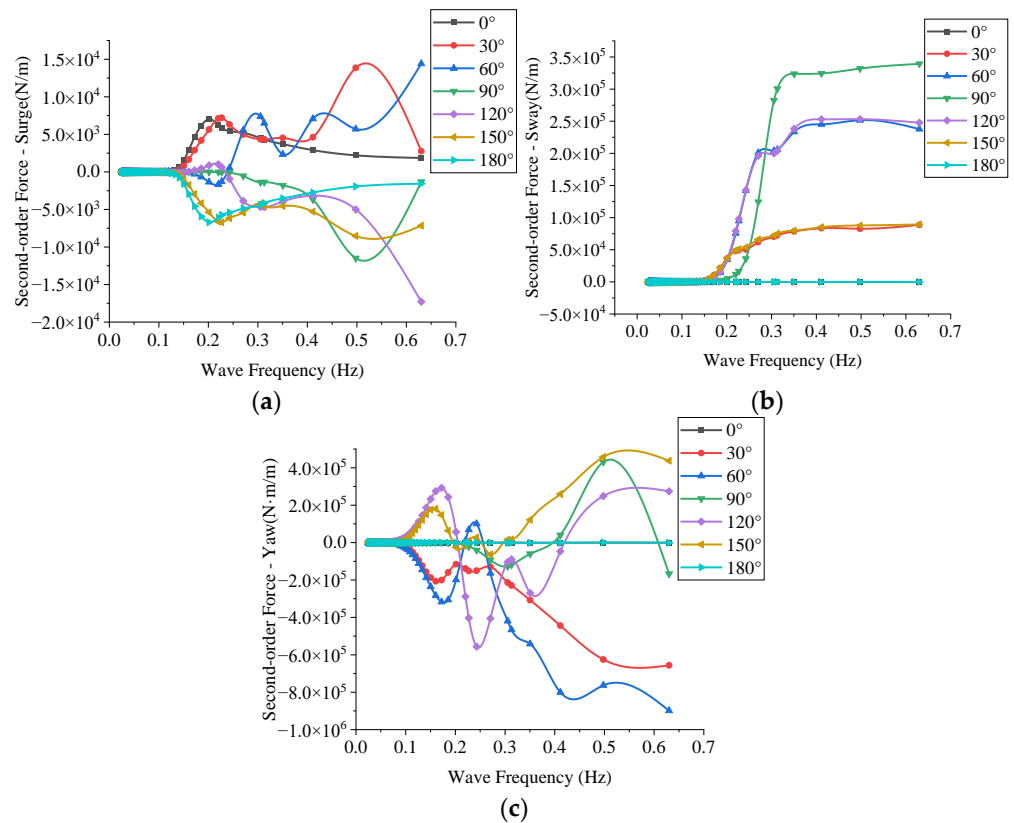


Figure 12. First-order force transfer function. (a) surge; (b) sway; (c) heave; (d) roll; (e) pitch; (f) yaw.

The second-order drift forces have a significant influence on the horizontal motion of the AAMV, which are zero in the three components of heave, roll, and pitch and only exist in the three components of surge, sway, and yaw. They are the main reason for altering the heading angle and path.

Figure 13 illustrates the results of the second-order force transfer functions for different incidence angles. The forces tend to zero in the low-frequency phase. When the frequency exceeds 0.16 Hz, it begins to affect the AAMV. In the range of sea states studied in this paper, the wave frequencies fall between 0.227 Hz and 0.505 Hz, implying that the AAMV will be affected by the second-order force during navigation. Due to the coupling effect of the structure, the second-order forces appear near numerous peaks with frequency and wave direction, and the mechanism is complex.



**Figure 13.** Second-order force transfer function. (a) surge; (b) sway; (c) yaw.

According to the calculations above, the wind and wave disturbance forces on the AAMV can be expressed as a function in Equation (18) [34].

$$F_w = A \cos(\omega_e t + \delta) \tag{18}$$

where  $\omega_e$  represents the encounter frequency.

The wind and wave disturbance forces in Equation (18) can be expressed using Equation (19).

$$F_w = \begin{bmatrix} \text{Re} [\zeta_A E_1 e^{i\omega t}] \\ \text{Re} [\zeta_A E_2 e^{i\omega t}] \\ \text{Re} [\zeta_A E_3 e^{i\omega t}] \\ \text{Re} [\zeta_A E_4 e^{i\omega t}] \\ \text{Re} [\zeta_A E_5 e^{i\omega t}] \\ \text{Re} [\zeta_A E_6 e^{i\omega t}] \end{bmatrix} \tag{19}$$

where  $\zeta_A$  represents the wave amplitude of the incident wave, while  $E_i$  represents the transfer amplitude of wind and wave disturbance forces.

Equation (18) can be expressed using Equation (20) to determine parameter  $A$ .

$$A = \zeta_A E_i (i = 1, 2, \dots, 6) \tag{20}$$

The mathematical expression for the disturbance force under the action of irregular wind and waves is shown in Equation (21). This expression is derived by adopting a statistical method and assuming that the irregular wave is a superposition of countless unit regular waves with different wave heights and wavelengths.

$$F_w = \sum_{i=1}^N A_i \cos(\omega_{ei}t + \delta_i) \tag{21}$$

#### 4. Stability Model

In this section, the 6-DOF motion model of the AAMV is decoupled into longitudinal motion equations (surge–pitch–sway in the longitudinal plane) and lateral motion equations (sway–roll–bow in the horizontal plane). The coupling effect between these two sets of equations is ignored. The small-perturbation theory is employed to derive the longitudinal and lateral first-order linear perturbation equations of the AAMV, which are applicable to the stability analysis of the AAMV under the combined effect of wind and waves. The wind and wave turbulence forces under different sea conditions are employed as the input turbulence to solve the motion response of the AAMV, thereby enabling the investigation of the change rule of the motion response under different sea conditions and different initial states.

##### 4.1. Longitudinal Stability Model

The longitudinal stability of the AAMV is determined by its coupled motions in three degrees of freedom: surge, heave, and pitch. To derive the longitudinal perturbation equation of the AAMV, the small-perturbation theory is employed, as shown in Equation (22).

$$\mathbf{D}_0 \begin{bmatrix} \Delta \dot{V} \\ \Delta \dot{\omega}_y \\ \Delta \dot{\alpha} \\ \Delta \dot{\theta} \\ \Delta \dot{z} \end{bmatrix} = \mathbf{A}_0 \begin{bmatrix} \Delta V \\ \Delta \omega_y \\ \Delta \alpha \\ \Delta \theta \\ \Delta z \end{bmatrix} + \mathbf{b}_0 \begin{bmatrix} \text{Re} [e^{i\omega t}] \\ \text{Re} [e^{i\omega t}] \\ \text{Re} [e^{i\omega t}] \\ 0 \\ 0 \end{bmatrix} \tag{22}$$

where,

$$\mathbf{D}_0 = \begin{bmatrix} (m + \lambda_{11}) \cos \alpha_0 & 0 & -(m + \lambda_{11})V_0 \sin \alpha_0 & 0 & 0 \\ (m + \lambda_{33}) \sin \alpha_0 & \lambda_{35} & (m + \lambda_{33})V_0 \cos \alpha_0 & 0 & 0 \\ \lambda_{35} \sin \alpha_0 & I_{yy} + \lambda_{55} & \lambda_{35}V_0 \cos \alpha_0 & 0 & 0 \\ 0 & 0 & 0 & 1 & 0 \\ 0 & 0 & 0 & 0 & 1 \end{bmatrix} \tag{23}$$

$$\mathbf{b}_0 = [E_1 \zeta_A \quad E_3 \zeta_A \quad E_5 \zeta_A \quad 0 \quad 0]^T \tag{24}$$

$$\mathbf{A}_0 = \begin{bmatrix} a_{11} & a_{12} & (B - G) \cos \theta_0 & 0 & 0 \\ a_{21} & a_{22} & (B - G) \sin \theta_0 & a_{24} & 0 \\ a_{31} & a_{32} & -Bz_c \cos \theta_0 & a_{34} & 0 \\ 0 & 1 & 0 & 0 & 0 \\ \sin 2\theta_0 & 0 & 0 & 2V_0 \cos 2\theta_0 & 0 \end{bmatrix} \tag{25}$$

where,

$$a_{11} = -\rho S C_x^\alpha V_0 - \rho_a S_a C_{xa}^\alpha V_0$$

$$a_{21} = \rho S V_0 (C_z^{\omega_y} + C_z^\alpha) + \rho_a S_a V_0 (C_{za}^{\omega_y} + C_{za}^\alpha)$$



$$\begin{aligned}
 a_{31} &= \rho SLV_0(m_y^{\omega_y} + m_y^\alpha) + \rho_a S_a l_a V_0(m_{ya}^{\omega_y} + m_{ya}^\alpha) - (\lambda_{11} - \lambda_{33})V_0 \sin 2\alpha_0 \\
 a_{12} &= -(m + \lambda_{33})V_0 \sin \alpha_0 \\
 a_{22} &= \frac{1}{2}\rho SV_0^2 C_z^{\omega_y} + \frac{1}{2}\rho_a S_a V_0^2 C_{za}^{\omega_y} - (m + \lambda_{11})V_0 \cos \alpha_0 \\
 a_{32} &= \frac{1}{2}\rho SLV_0^2 m_y^{\omega_y} + \frac{1}{2}\rho_a S_a l_a V_0^2 m_{ya}^{\omega_y} \\
 a_{24} &= \frac{1}{2}\rho SV_0^2 C_z^\alpha + \frac{1}{2}\rho_a S_a V_0^2 C_{za}^\alpha \\
 a_{34} &= -(\lambda_{11} - \lambda_{33})V_0^2 \cos 2\alpha_0 + \lambda_{35}V_0 \omega_{y0} \sin \alpha_0
 \end{aligned}$$

Equation (22) can be expressed as the longitudinal state-space equation:

$$\begin{cases} \dot{x} = \mathbf{A}x + \mathbf{b}\text{Re}[e^{i\omega t}] \\ y = \mathbf{c}x \end{cases} \tag{26}$$

where  $x$  is the longitudinal state vector:

$$x = [\Delta V \quad \Delta \omega_y \quad \Delta \alpha \quad \Delta \theta \quad \Delta z]^T \tag{27}$$

$\mathbf{A}$  is the longitudinal state matrix:

$$\mathbf{A} = \mathbf{D}_0^{-1}\mathbf{A}_0 \tag{28}$$

$\mathbf{b}$  is the longitudinal input state matrix:

$$\mathbf{b} = \mathbf{D}_0^{-1}\mathbf{b}_0 \tag{29}$$

$\mathbf{c}$  is the 4-order unit matrix.

This paper focuses on the stability of the AAMV in wind and waves, specifically its motion response to wind and wave disturbance forces. These forces are continuous inputs with functional expression in the time domain, as shown in Equation (30).

$$\text{Re}[e^{i\omega t}] = R_{eg}(t) = \begin{cases} 0, t < 0 \\ \cos(\omega t), t \geq 0 \end{cases} \tag{30}$$

Equation (31) is obtained by applying the Laplace transform to the above equation.

$$R_{eg}(s) = \frac{s}{s^2 + \omega^2} \tag{31}$$

The motion response of the AAMV to wind and waves is determined by the relationship between the output of its longitudinal motion vector  $x$  and the input of wind and wave disturbance. The relationship can be expressed as Equation (32).

$$\begin{cases} y(s) = \mathbf{G}(s)R_{eg} \\ \mathbf{G}(s) = \mathbf{c}(s\mathbf{I} - \mathbf{A})^{-1}\mathbf{b} \end{cases} \tag{32}$$

where  $\mathbf{G}(s)$  is the transfer function matrix of the system, which can be expressed as follows:

$$\mathbf{G}(s) = [g_1(s) \quad g_2(s) \quad g_3(s) \quad g_4(s)]^T \tag{33}$$

where  $g_i(s)$  is the  $i$ th output variable function.

Thus, the response function of the motion parameters can be obtained, as shown in Equation (34).

$$\begin{aligned}
 \Delta V(s) &= \frac{g_1(s)s}{s^2 + \omega^2} \\
 \Delta q(s) &= \frac{g_2(s)s}{s^2 + \omega^2} \\
 \Delta \alpha(s) &= \frac{g_3(s)s}{s^2 + \omega^2} \\
 \Delta \theta(s) &= \frac{g_4(s)s}{s^2 + \omega^2}
 \end{aligned} \tag{34}$$

The transition–timing–function of the motion parameters in the time domain can be obtained by applying the inverse Laplace transform to Equation (34), as demonstrated in Equation (35).

$$\begin{aligned}
 \Delta V(t) &= \downarrow^{-1}(\Delta V(s)) = \downarrow^{-1} \frac{g_1(s)s}{s^2 + \omega^2} \\
 \Delta q(t) &= \downarrow^{-1}(\Delta q(s)) = \downarrow^{-1} \frac{g_2(s)s}{s^2 + \omega^2} \\
 \Delta \alpha(t) &= \downarrow^{-1}(\Delta \alpha(s)) = \downarrow^{-1} \frac{g_3(s)s}{s^2 + \omega^2} \\
 \Delta \theta(t) &= \downarrow^{-1}(\Delta \theta(s)) = \downarrow^{-1} \frac{g_4(s)s}{s^2 + \omega^2}
 \end{aligned}
 \tag{35}$$

#### 4.2. Lateral Stability Model

The lateral stability of the AAMV involves coupled motions in three degrees of freedom: sway, roll, and yaw. Similarly, its lateral perturbation equations are derived using small-perturbation theory, as shown in Equation (36).

$$\mathbf{D}_1 \begin{bmatrix} \Delta \dot{V} \\ \Delta \dot{\omega}_x \\ \Delta \dot{\omega}_z \\ \Delta \dot{\beta} \\ \Delta \dot{\phi} \\ \Delta \dot{\psi} \end{bmatrix} = \mathbf{A}_1 \begin{bmatrix} \Delta V \\ \Delta \omega_x \\ \Delta \omega_z \\ \Delta \beta \\ \Delta \phi \\ \Delta \psi \end{bmatrix} + \mathbf{b}_1 \begin{bmatrix} \operatorname{Re} [e^{i\omega t}] \\ \operatorname{Re} [e^{i\omega t}] \\ \operatorname{Re} [e^{i\omega t}] \\ \operatorname{Re} [e^{i\omega t}] \\ 0 \\ 0 \end{bmatrix}
 \tag{36}$$

where,

$$\mathbf{D}_1 = \begin{bmatrix} (m + \lambda_{11}) \cos \beta_0 & 0 & 0 & -(m + \lambda_{11})V_0 \sin \beta_0 & 0 & 0 \\ (m + \lambda_{22}) \sin \beta_0 & -mz_G + \lambda_{24} & \lambda_{26} & (m + \lambda_{22})V_0 \cos \beta_0 & 0 & 0 \\ \lambda_{24} \sin \beta_0 & I_{xx} + \lambda_{44} & \lambda_{46} & \lambda_{24}V_0 \cos \beta_0 & 0 & 0 \\ \lambda_{26} \sin \beta_0 & 0 & I_{zz} + \lambda_{66} & \lambda_{26}V_0 \cos \beta_0 & 0 & 0 \\ 0 & 0 & 0 & 0 & 1 & 0 \\ 0 & 0 & 0 & 0 & 0 & 1 \end{bmatrix}
 \tag{37}$$

$$\mathbf{b}_1 = [E_1 \zeta_A \quad E_2 \zeta_A \quad E_4 \zeta_A \quad E_6 \zeta_A \quad 0 \quad 0]^T
 \tag{38}$$

$$\mathbf{A}_1 = \begin{bmatrix} 0 & 0 & a_{13} & 0 & 0 & 0 \\ a_{21} & 0 & a_{23} & a_{24} & (B - G) \cos \phi_0 & 0 \\ a_{31} & a_{32} & 0 & 0 & -B(z_c \cos \phi_0 + y_c \sin \phi_0) & 0 \\ a_{41} & a_{42} & a_{43} & a_{44} & Bx_c \cos \phi_0 & 0 \\ 0 & 1 & 0 & 0 & 0 & 0 \\ 0 & 0 & \cos \phi_0 & 0 & 0 & 0 \end{bmatrix}
 \tag{39}$$

where,

$$\begin{aligned}
 a_{21} &= \rho SV_0 (C_y^\beta + C_y^{\omega_z}) + \rho_a S_a V_0 (C_{ya}^\beta + C_{ya}^{\omega_z}) \\
 a_{31} &= \rho SV_0 L m_x^{\omega_x} \omega_x + \rho_a S_a V_0 B_a m_{xi}^{\omega_x} \omega_x \\
 a_{41} &= \rho SV_0 L (m_z^{\omega_z} \omega_z + m_z^\beta \beta) + \rho_a S_a V_0 B_a (m_{za}^{\omega_z} \omega_z + m_{za}^\beta \beta) + (\lambda_{11} - \lambda_{22})V_0 \sin 2\beta_0 \\
 a_{32} &= \frac{1}{2} \rho SV_0^2 L m_x^{\omega_x} + \frac{1}{2} \rho_a S_a V_0^2 B_a m_{xa}^{\omega_x} \\
 a_{42} &= -\lambda_{24} V_0 \cos \beta_0 \\
 a_{13} &= -(m + \lambda_{22})V_0 \sin \beta_0 \\
 a_{23} &= \frac{1}{2} \rho SV_0^2 C_y^{\omega_z} + \frac{1}{2} \rho_a S_a V_0^2 C_{ya}^{\omega_z} - (m + \lambda_{11})V_0 \cos \beta_0 \\
 a_{43} &= \frac{1}{2} \rho SV_0^2 L m_z^{\omega_z} + \frac{1}{2} \rho_a S_a V_0^2 B_a m_{za}^{\omega_z} - \lambda_{26} V_0 \cos \beta_0 \\
 a_{24} &= \frac{1}{2} \rho SV_0^2 C_y^\beta + \frac{1}{2} \rho_a S_a V_0^2 C_{ya}^\beta
 \end{aligned}$$

$$a_{44} = \frac{1}{2}\rho S V_0^2 L m_z^\beta + \frac{1}{2}\rho_a S_a V_0^2 B_a m_{za}^\beta - (\lambda_{11} - \lambda_{22}) V_0^2 \cos 2\beta_0$$

Similarly, Equation (36) can also be expressed as the lateral state-space formula:

$$\begin{cases} \dot{x} = \mathbf{C}x + \mathbf{d}^T \text{Re}[e^{i\omega t}] \\ y = \mathbf{e}x \end{cases} \quad (40)$$

where  $x$  is the lateral state vector:

$$x = [\Delta V \quad \Delta\omega_x \quad \Delta\omega_z \quad \Delta\beta \quad \Delta\phi \quad \Delta\psi]^T \quad (41)$$

$\mathbf{C}$  is the lateral state matrix:

$$\mathbf{C} = \mathbf{D}_1^{-1} \mathbf{A}_1 \quad (42)$$

$\mathbf{d}$  is the lateral input state matrix:

$$\mathbf{d} = \mathbf{D}_1^{-1} \mathbf{b}_1 \quad (43)$$

$\mathbf{e}$  is the 6-order unit matrix.

Equation (44) shows the response function of the lateral motion parameters of the AAMV.

$$\begin{aligned} \Delta V(s) &= \frac{g_1(s)s}{s^2 + \omega^2} & \Delta p(s) &= \frac{g_2(s)s}{s^2 + \omega^2} & \Delta r(s) &= \frac{g_3(s)s}{s^2 + \omega^2} \\ \Delta\beta(s) &= \frac{g_4(s)s}{s^2 + \omega^2} & \Delta\phi(s) &= \frac{g_5(s)s}{s^2 + \omega^2} & \Delta\psi(s) &= \frac{g_6(s)s}{s^2 + \omega^2} \end{aligned} \quad (44)$$

The transition–timing–function for the lateral motion parameters is displayed in Equation (45).

$$\begin{cases} \Delta V(t) = \uparrow^{-1}(\Delta V(s)) = \uparrow^{-1} \frac{g_1(s)s}{s^2 + \omega^2} \\ \Delta p(t) = \uparrow^{-1}(\Delta p(s)) = \uparrow^{-1} \frac{g_2(s)s}{s^2 + \omega^2} \\ \Delta r(t) = \uparrow^{-1}(\Delta r(s)) = \uparrow^{-1} \frac{g_3(s)s}{s^2 + \omega^2} \\ \Delta\beta(t) = \uparrow^{-1}(\Delta\beta(s)) = \uparrow^{-1} \frac{g_4(s)s}{s^2 + \omega^2} \\ \Delta\phi(t) = \uparrow^{-1}(\Delta\phi(s)) = \uparrow^{-1} \frac{g_5(s)s}{s^2 + \omega^2} \\ \Delta\psi(t) = \uparrow^{-1}(\Delta\psi(s)) = \uparrow^{-1} \frac{g_6(s)s}{s^2 + \omega^2} \end{cases} \quad (45)$$

## 5. Stability Analysis

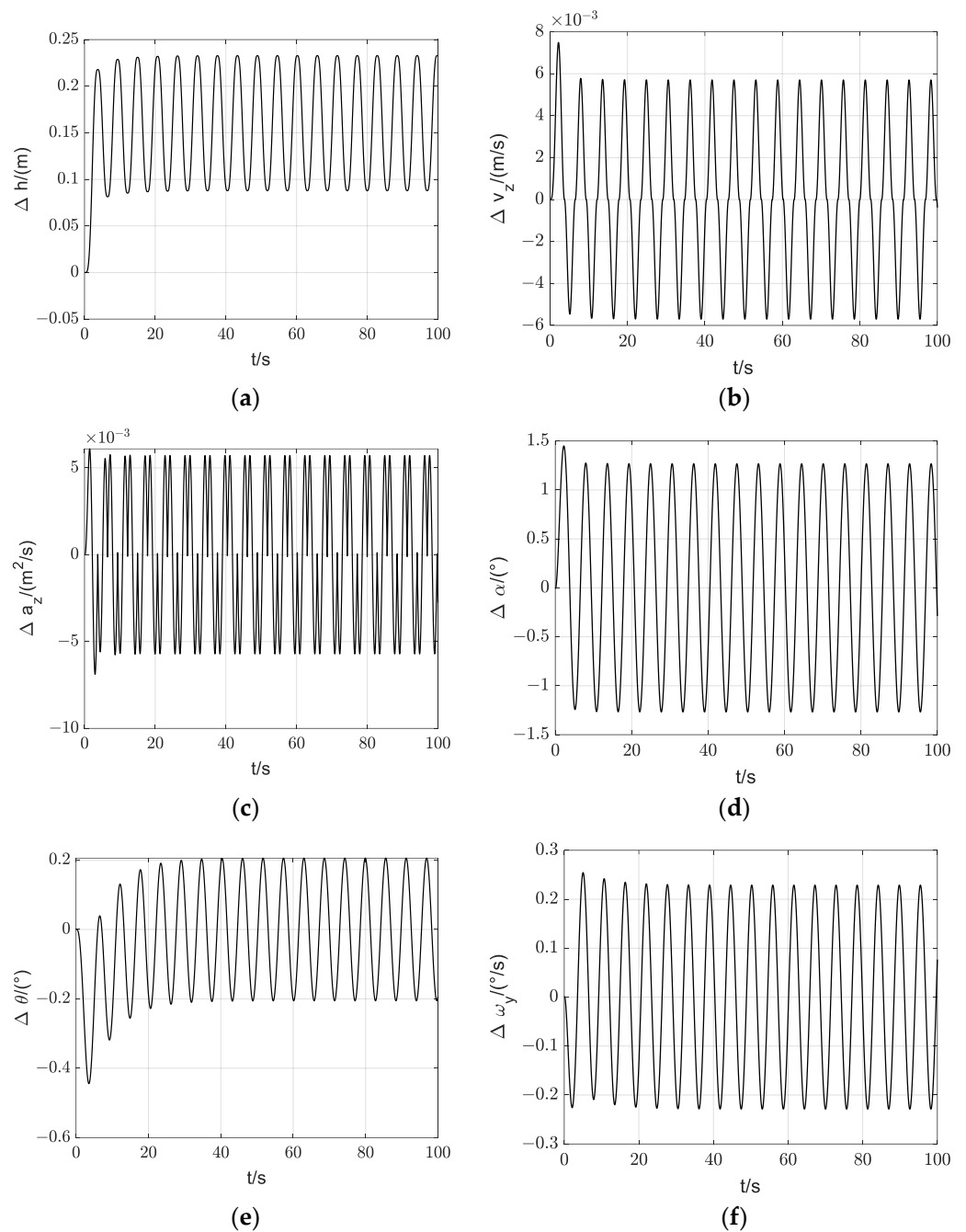
### 5.1. Longitudinal Stability

The longitudinal motion response characteristics of the AAMV under the action of regular and irregular wind and waves are analyzed based on the above analysis. The results are presented in Figures 14 and 15, respectively.

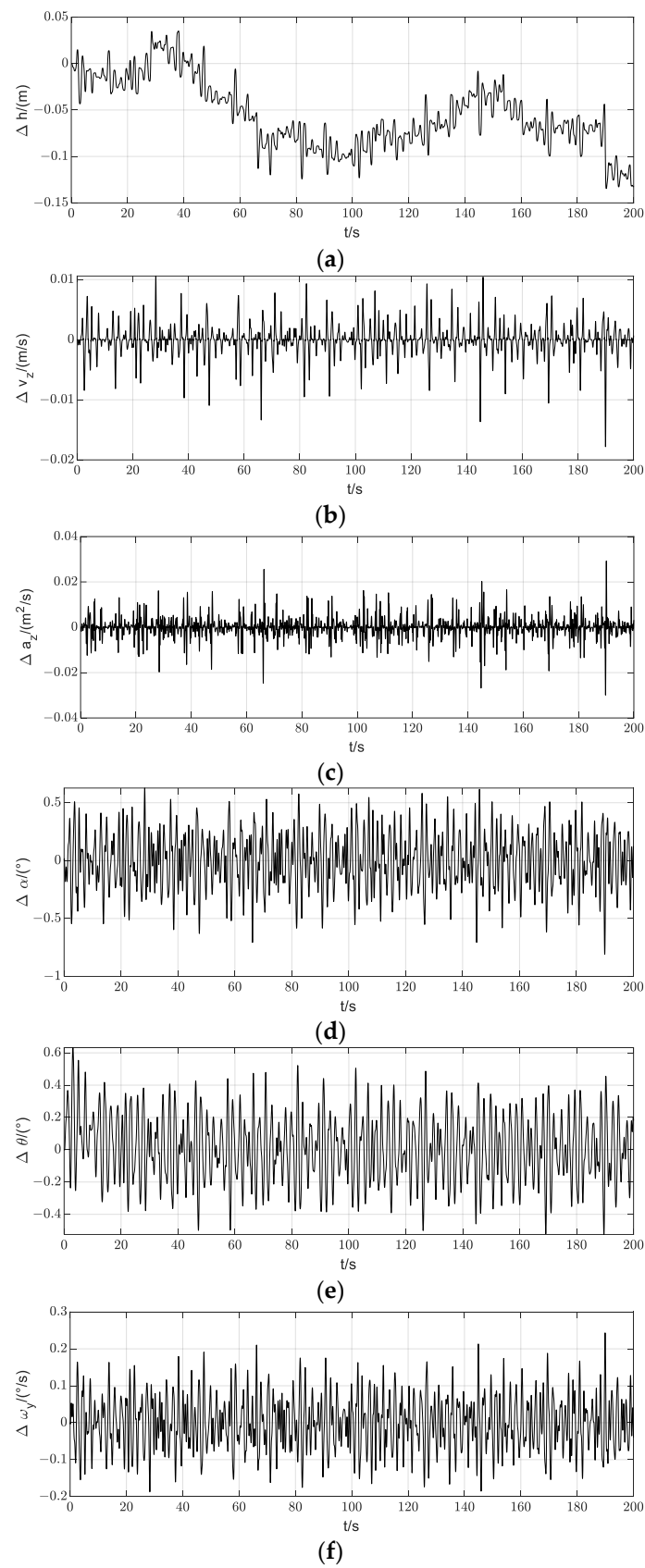
Figure 14 displays the longitudinal motion response curve of the AAMV in wind and waves at  $Fr_B = 6.7$  under the class V sea state. When wind and waves disturb the AAMV, each motion parameter fluctuates to a different degree, causing the AAMV to leave its original equilibrium state. After a transitional period, each motion parameter exhibits periodic oscillation with a certain amplitude, and the AAMV enters a new dynamic equilibrium state. The time required for the heave and pitch angles to transition to the new equilibrium state is relatively long. Additionally, the amplitudes of the heave and pitch responses are 0.0734 m and  $0.210^\circ$ , respectively. These results suggest that at the design speed, the AAMV will depart from its original non-acceleration linear motion state when disturbed by the wind and waves of the class V sea state. However, it will eventually enter a dynamic equilibrium state with good stability.

Figure 15 displays the time–domain curve of the motion response of the AAMV in irregular wind and waves under the same conditions as Figure 14. When the AAMV is exposed to irregular wind and waves, its motion parameters exhibit irregular fluctuations, and the amplitude of the fluctuations is essentially consistent with the motion response

amplitude in regular wind and waves. This suggests that the AAMV will remain relatively stable even when perturbed by wind and waves in a class V sea state.



**Figure 14.** Response curves for longitudinal motion in regular waves. (a) heave response curve; (b) heave velocity response curve; (c) heave acceleration response curve; (d) angle of attack response curve; (e) pitch angle response curve; (f) pitch angular velocity response curve.



**Figure 15.** Response curves for longitudinal motion in irregular waves. (a) heave response curve; (b) heave velocity response curve; (c) heave acceleration response curve; (d) angle of attack response curve; (e) pitch angle response curve; (f) pitch angular velocity response curve.

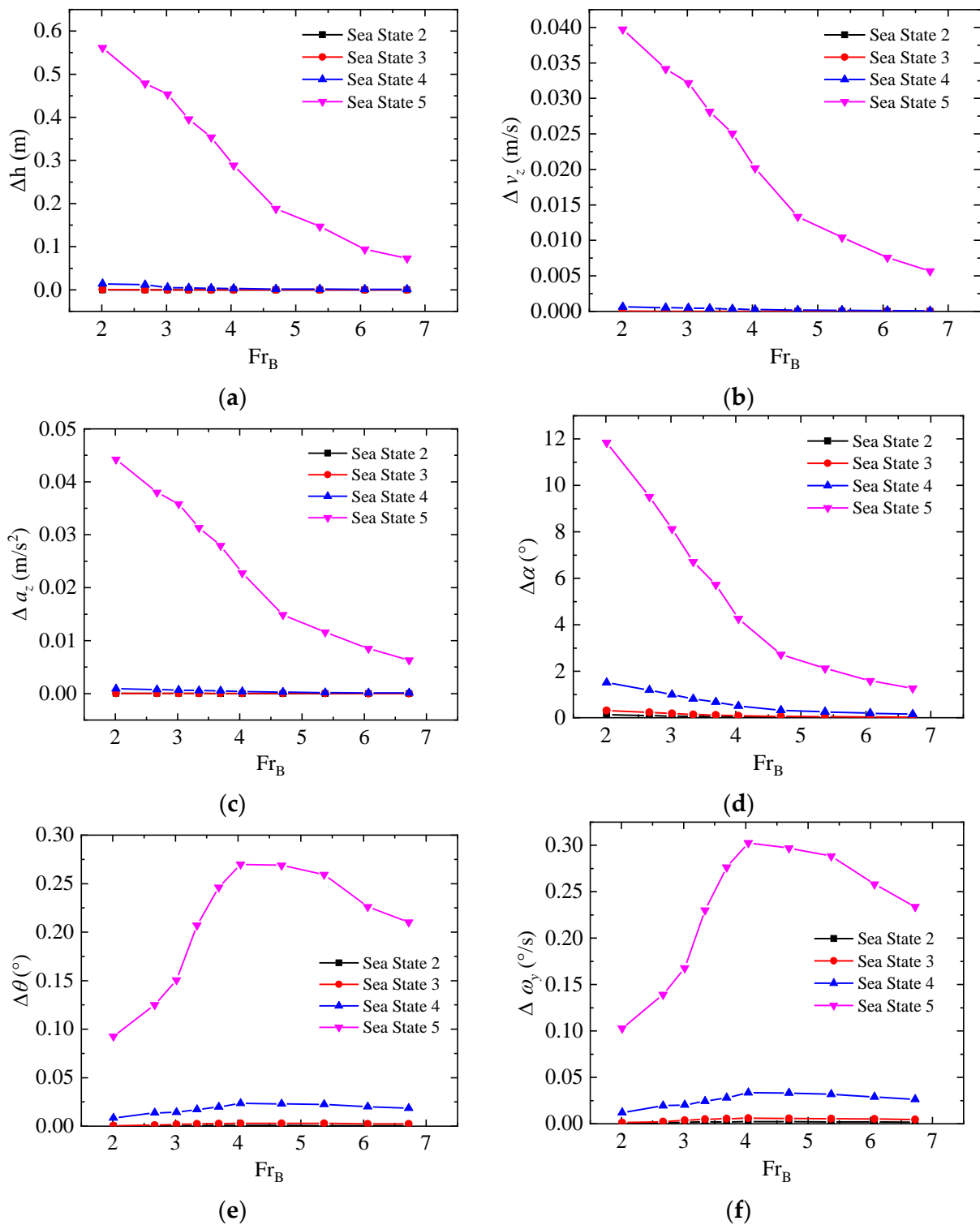
Figure 16a–c presents the response amplitudes of the AAMV in terms of heave  $\Delta h$ , heave velocity  $\Delta v_z$ , and heave acceleration  $\Delta a_z$  under different sea states and  $Fr_B$ . The vertical motion of the AAMV is minimally affected by wind and wave disturbances in low-sea states. As the class of sea state increases, the response amplitudes  $\Delta h$ ,  $\Delta v_z$ , and  $\Delta a_z$  increase. Additionally, the response of the motion to wind and wave disturbances will vary depending on the  $Fr_B$  value. An increase in the  $Fr_B$  leads to a gradual decrease in the response amplitudes of  $\Delta h$ ,  $\Delta v_z$ , and  $\Delta a_z$  in waves. At  $Fr_B = 2$ ,  $\Delta h$  in a class V sea state is 0.561 m, and the AAMV shows subpar seakeeping performance with a  $\Delta h$  of 0.561 m. When the  $Fr_B$  increases to 6.7, the aerodynamic lift increases rapidly with the speed, and the aerodynamically alleviated effect becomes progressively significant. The AAMV experiences a drastic detachment from the water surface under the influence of aerodynamic alleviation. Only a small portion of the planing surface glides rapidly on the wave surface, resulting in decreased wave influence. As a result,  $\Delta h$  in a class V sea state reduces to 0.0734 m,  $\Delta v_z$  reduces to 0.00568 m/s, and  $\Delta a_z$  reduces to 0.00633 m/s<sup>2</sup>, which significantly diminishes the extent of the AAMV's heave motion in waves, thereby enhancing its heave stability in waves.

Figure 16d displays the response amplitude of the AAMV in terms of the angle of attack  $\Delta\alpha$  under different sea states and  $Fr_B$ . The trend of  $\Delta\alpha$  with sea state class and  $Fr_B$  is consistent with its vertical motion variation: as the sea state class increases and the  $Fr_B$  decreases, the response amplitude of the angle of attack also increases. It is worth noting that  $\Delta\alpha$  reaches as high as 14° under a high sea state and low  $Fr_B$ , which indicates a large angle of attack. Although the low-speed state is not the intended operational state of the AAMV, the resistance and lift of the AAMV will exhibit a pronounced nonlinearity at a large angle of attack. This phenomenon should be a focus of future research.

Figure 16e,f displays the response amplitude of the AAMV in terms of pitch angle  $\Delta\theta$ , pitch angular velocity  $\Delta\omega_y$  at varying sea states, and  $Fr_B$ . The response amplitude of pitch angle in wind and waves shows a tendency to first increase and then decrease with  $Fr_B$ . The pitch angle response amplitude peaks when  $Fr_B$  increases to 4.04, with a maximum amplitude of 0.270° in a class V sea state, showing a slight oscillatory trend. With the further increase in  $Fr_B$ , the AAMV enters the high-speed planing phase, and its pitch angle and angular velocity response in the wind and waves show a continuous decreasing trend. With regard to the impact of sea state on the pitch motion of the AAMV, it can be observed that its law aligns with the principle of heave motion. This indicates that as the sea state class increases, the pitch motion parameters exhibit a correspondingly more pronounced response, which suggests a deterioration in pitch stability.

## 5.2. Lateral Stability

The lateral motion response characteristics of the AAMV under the action of regular and irregular wind and waves are analyzed based on the above analysis. The results are presented in Figures 17 and 18 ( $Fr_B = 6.7$ , class V sea state), respectively. Similarly, after being disturbed by regular wind and waves, the lateral motion parameters of the AAMV will respond to varying degrees, causing it to lose its current equilibrium state. However, after a transitional period, each motion parameter will exhibit sinusoidal oscillations with a certain amplitude, and the AAMV will reach a new dynamic equilibrium state. The amplitude of fluctuation in irregular wind and waves is also comparable to the motion response amplitude under regular wind and waves. The response amplitudes of roll angle, sideslip angle, directional angle, and yaw angle are 0.0229°, 0.128°, 0.159°, and 0.160°, respectively. Overall, the lateral stability is good.



**Figure 16.** The response amplitude to longitudinal motion in the presence of different sea states and  $Fr_B$ . (a) heave; (b) heave velocity; (c) heave acceleration; (d) angle of attack; (e) pitch angle; (f) pitch angular velocity.

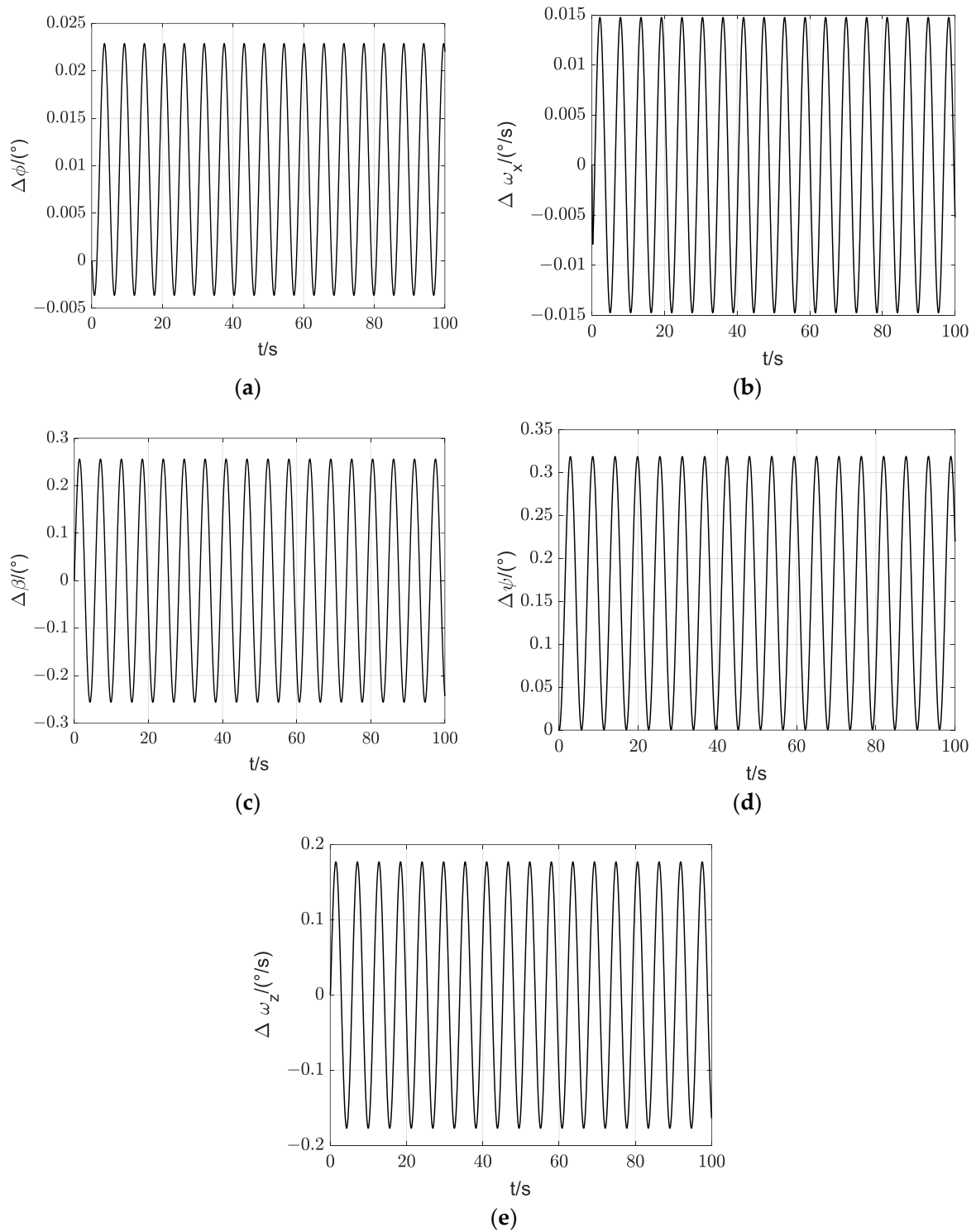


**Figure 17.** Response curves for lateral motion in regular waves. **(a)** roll angle response curve; **(b)** roll angular velocity response curve; **(c)** sideslip angle response curve; **(d)** yaw angle response curve; **(e)** yaw angular velocity response curve.



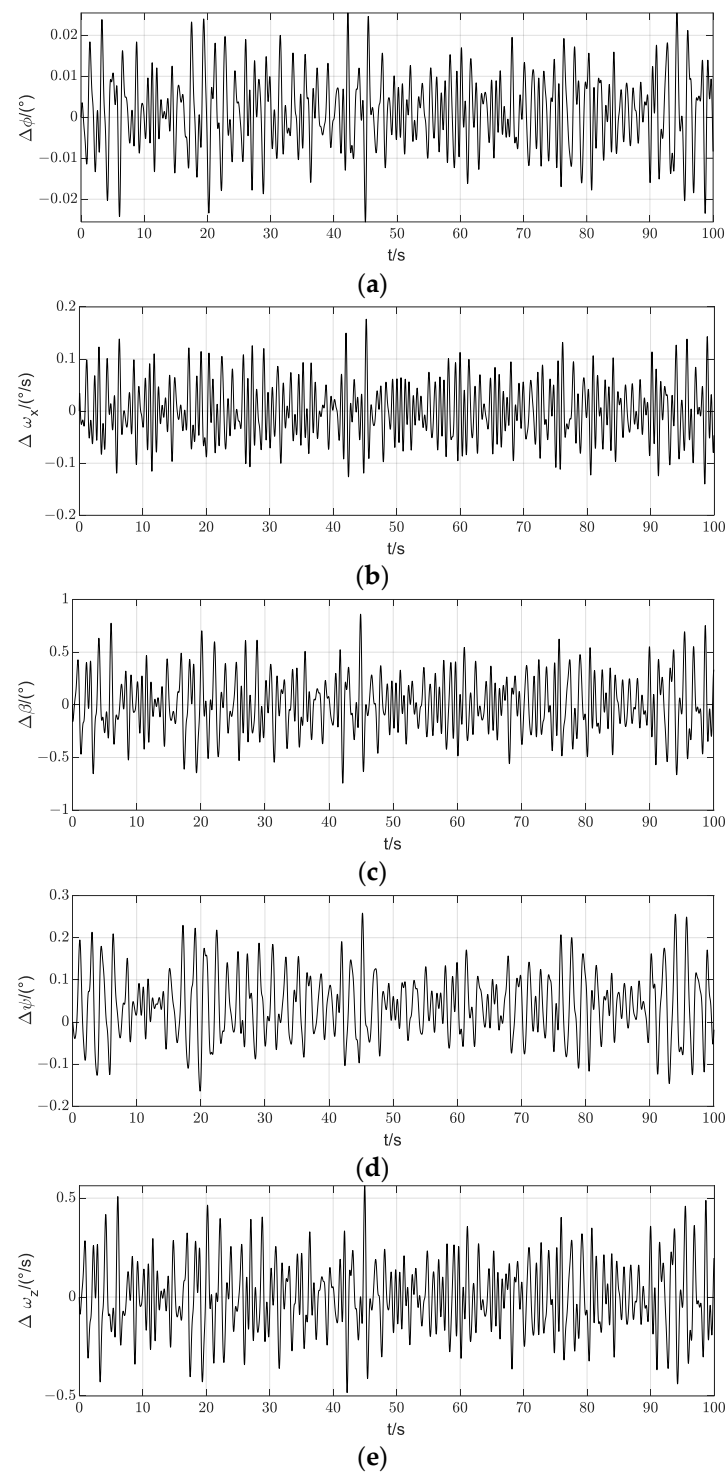


**Figure 18.** Response curves for lateral motion in irregular waves. (a) roll angle response curve; (b) roll angular velocity response curve; (c) sideslip angle response curve; (d) yaw angle response curve; (e) yaw angular velocity response curve.

Figure 19a,b presents the response amplitudes of the AAMV in terms of roll angle  $\Delta\phi$ , roll angular velocity  $\Delta\omega_x$  under different sea states, and  $Fr_B$ . As with heave stability, the response amplitude of the AAMV's roll angle and angular velocity in waves diminishes markedly with increasing  $Fr_B$ . This suggests that the impact of waves on the AAMV's roll motion is significantly diminished due to the aerodynamic alleviation during the high-speed planing phase. Furthermore, an increase in sea state class will exacerbate the roll

motion instability of the AAMV. In the high-speed planing phase, the floats on both sides of the wing are detached from the water. When the roll motion occurs, the floats are partially immersed in the water to generate the restoring moment, which reduces the roll angle. This restoring moment is also present in the low-speed phase. When  $Fr_B = 2$ , the maximum amplitudes of the roll angle and its angular velocity are  $0.540^\circ$  and  $0.517^\circ/s$ , respectively, at sea state V. This suggests that the roll motion generated by wind and wave action does not pose a risk of rollover at any speed. The roll stability of the AAMV is good.

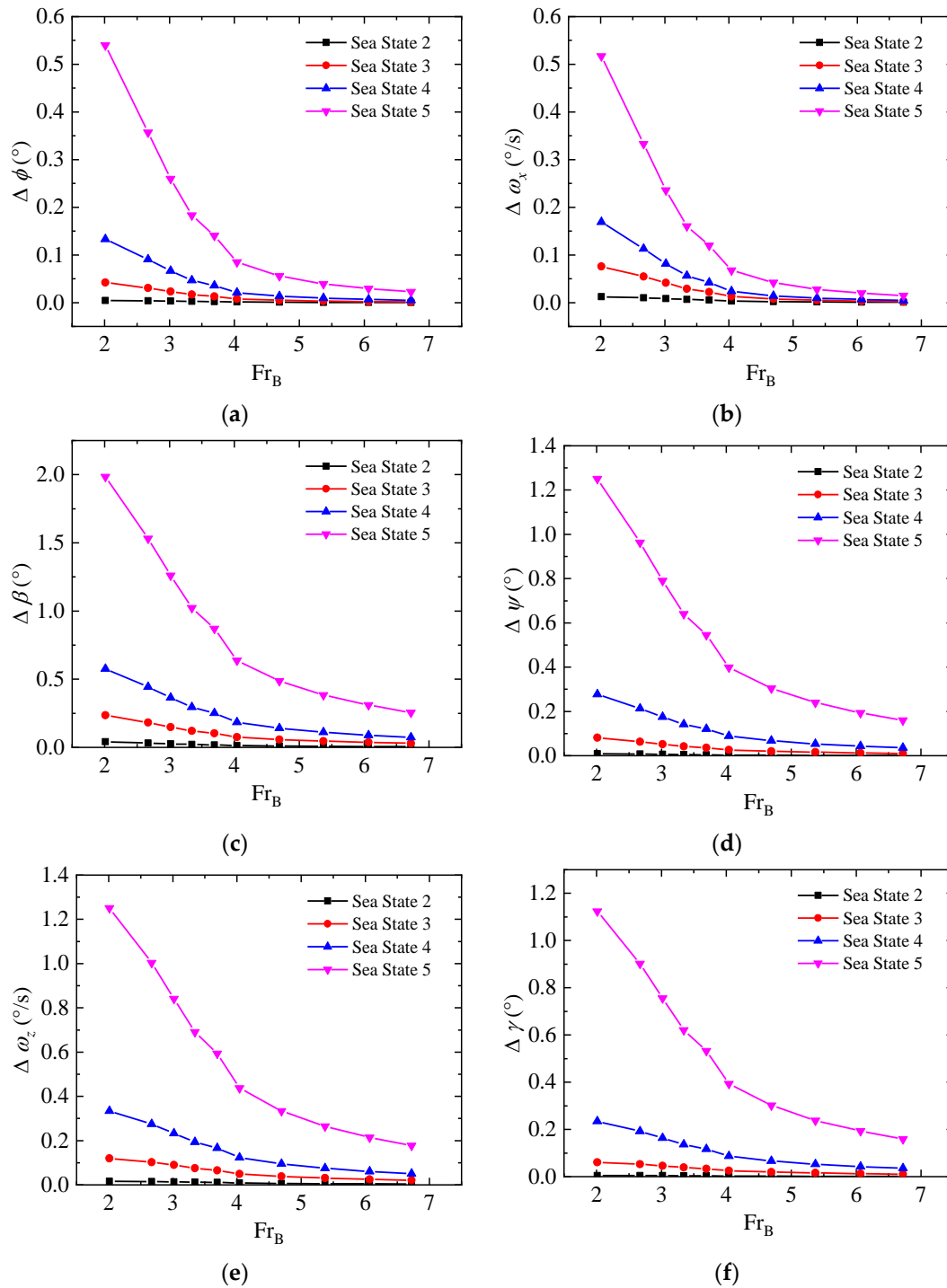


**Figure 19.** The response amplitude to lateral motion in the presence of different sea states and  $Fr_B$ . (a) roll angle; (b) roll angular velocity; (c) sideslip angle; (d) yaw angle; (e) yaw angular velocity; (f) directional angle.

Figure 19c–f presents the response amplitudes of the AAMV in terms of directional stability parameters (including sideslip angle  $\beta$ , yaw angular velocity  $\omega_z$ , yaw angle  $\psi$ , and directional angle  $\gamma$ ) of the AAMV with  $Fr_B$  in different sea states. The directional stability of the AAMV can be analyzed based on this information, with the observed trend bearing resemblance to that of roll stability. In the context of the design speed and class V sea state, the response amplitude of the sideslip angle  $\Delta\beta$  is  $0.256^\circ$ , the response amplitude of the yaw angular velocity  $\Delta\omega_z$  is  $0.177^\circ/\text{s}$ , the response amplitude of the yaw angle  $\Delta\psi$  is  $0.159^\circ$ , and the response amplitude of the direction angle  $\Delta\gamma$  is  $0.160^\circ$ . The aforementioned outcomes demonstrate that the directional stability of the AAMV is satisfactory.

## 6. Conclusions

The principal objective of this study is to provide a reference for the stability analysis of the AAMV in waves. This paper investigates the effects of different sea states and speeds on the 6-DOF motion response of the AAMV.

This paper considers the equal importance of aerodynamic and hydrodynamic forces and establishes the 6-DOF motion equations, considering aerodynamic alleviation. Based on the small-perturbation theory, the linear perturbation equations of the AAMV are derived, and numerical investigations are carried out to investigate the longitudinal and lateral stability of the AAMV in regular and irregular waves. This provides a more comprehensive and preliminary exploration of the AAMVs' stability in waves.

A numerical model of wave loads considering viscous corrections has been developed based on the potential theory. The simulation results based on this model are significantly comparable to those based on CFD, thus identifying an appropriate numerical modeling approach that can be used as a reference for the AAMV. The model can be employed to further analyze the forces and motions of AAMVs in waves.

The results of the study indicate that the primary impact of first-order wave forces on the AAMV is longitudinal motion, whereas second-order wave forces are the predominant driver of horizontal plane motion, such as heading. With regard to stability, the AAMV exhibits periodic movement in conjunction with the waves. Due to the aerodynamically alleviated effect, the AAMV is substantially detached from the water surface during the high-speed planing phase, which effectively reduces the influence of waves on its motion stability. Furthermore, the increase in the aerodynamic force can effectively enhance its restoring moment. Consequently, as speed increases, the AAMV's motion stability improves in accordance with this increase. The possibility of destabilization under the same sea state also decreases. At cruising speed, the pitch response amplitude of the AAMV is  $0.210^\circ$ , the roll response amplitude is  $0.0229^\circ$ , and the heave response amplitude is  $0.0734\text{ m}$  in a class V sea state. The findings offer insight into the stability change rule of the AAMV, specifically in relation to the transition from low-speed acceleration to cruise speed. The conclusions of this study can inform further optimization of the AAMV configuration.

The stability analysis accuracy of the AAMV is strongly related to the hydrodynamic forces to which it is subjected. Consequently, improving the forecasting accuracy of hydrodynamic parameters is important for the future. Furthermore, this paper facilitates the computation, decoupling, and linearization of the motion model. Based on this, a preliminary analysis of the stability of the AAMV is carried out. Nevertheless, at low speeds, the larger motion amplitude serves to further accentuate the nonlinear characteristics, thereby necessitating further investigation into the nonlinear stability model of the 6-DOF coupled motion.

**Author Contributions:** Y.S.: Methodology, Analysis, Software, Writing—original draft. X.D.: Conceptualization, Funding acquisition, Writing—review and editing. Y.H.: Writing—review and editing. All authors have read and agreed to the published version of the manuscript.

**Funding:** The author(s) disclosed receipt of the following financial support for the research, authorship, and publication of this article: This work is supported by the National Natural Science Foundation of China (No. U2341217).

**Institutional Review Board Statement:** Not applicable.

**Informed Consent Statement:** Not applicable.

**Data Availability Statement:** The data are available from the corresponding author on reasonable request.

**Acknowledgments:** The authors would like to express their gratitude to the editor and reviewers for their constructive comments and suggestions, which have contributed to the enhancement of the paper's quality.

**Conflicts of Interest:** All authors declare no conflicts of interest.

## References

1. Kumar, Y.H.; Vijayakumar, R. Development of an Energy Efficient Stern Flap for Improved EEDI of a Typical High-Speed Displacement Vessel. *Def. Sci. J.* **2020**, *70*, 95–102. [[CrossRef](#)]
2. Goldhirsch, I.; Sulem, P.L.; Orszag, S.A. Stability and Lyapunov Stability of Dynamical Systems: A Differential Approach and a Numerical Method. *Phys. D Nonlinear Phenom.* **1987**, *27*, 311–337. [[CrossRef](#)]
3. Englar, R.J.; Gregory, S.D.; Ford, D.A. In-Ground-Effect Evaluation and Aerodynamic Development of Advanced Unlimited Racing Hydroplanes. In Proceedings of the 33rd Aerospace Sciences Meeting and Exhibit, Reno, NV, USA, 9–12 January 1995. [[CrossRef](#)]
4. Englar, R.J. Application of Advanced Aerodynamic Technology to Ground and Sport Vehicles. In Proceedings of the 26th AIAA Applied Aerodynamics Conference, Honolulu, HI, USA, 18–21 August 2008. [[CrossRef](#)]
5. Wang, L.; Yang, K.; Yue, T.; Liu, H. Wing-in-Ground Craft Longitudinal Modeling and Simulation Based on a Moving Wavy Ground Test. *Aerosp. Sci. Technol.* **2022**, *126*, 107605. [[CrossRef](#)]
6. Zou, J.; Lu, S.; Sun, H.; Zan, L.; Cang, J. Experimental Study on Motion Behavior and Longitudinal Stability Assessment of a Trimaran Planing Hull Model in Calm Water. *J. Mar. Sci. Eng.* **2021**, *9*, 164. [[CrossRef](#)]
7. Fossen, T.I. *Guidance and Control of Ocean Vehicles*; John Wiley & Sons: Hoboken, NJ, USA, 1994; p. 480.
8. Matveev, K.I. Modeling of Autonomous Hydrofoil Craft Tracking a Moving Target. *Unmanned Syst.* **2020**, *8*, 171–178. [[CrossRef](#)]
9. Sahin, O.S.; Kahramanoglu, E.; Cakici, F.; Pesman, E. Control of Dynamic Trim for Planing Vessels with Interceptors in Terms of Comfort and Minimum Drag. *Brodogr. Int. J. Nav. Archit. Ocean Eng. Res. Dev.* **2023**, *74*, 1–17. [[CrossRef](#)]
10. Collu, M.; Patel, M.; Trarieux, F. Aerodynamically Alleviated Marine Vehicles (AAMV): Development of a Mathematical Framework to Design High Speed Marine Vehicles with Aerodynamic Surfaces. In Proceedings of the International Conference on High Performance Marine Vehicles 2009 (HPMV09), Shanghai, China, 16–17 April 2009.
11. Collu, M.; Patel, M.H.; Trarieux, F. The Longitudinal Static Stability of an Aerodynamically Alleviated Marine Vehicle, a Mathematical Model. *Proc. R. Soc. Math. Phys. Eng. Sci.* **2010**, *466*, 1055–1075. [[CrossRef](#)]
12. Xu, S.; Chen, K.; Tang, Y.; Xiong, Y.; Ma, T.; Tang, W. Research on the Transverse Stability of an Air Cushion Vehicle Hovering over the Rigid Ground. *Ships Offshore Struct.* **2022**, *17*, 2300–2316. [[CrossRef](#)]
13. Vassalos, D.; Xie, N.; Jasionowski, A.; Konovessis, D. Stability and Safety Analysis of the Air-Lifted Catamaran. *Ships Offshore Struct.* **2008**, *3*, 91–98. [[CrossRef](#)]
14. Amiri, M.M.; Dakhrabadi, M.T.; Seif, M.S. Development of a Semi-Empirical Method for Hydro-Aerodynamic Performance Evaluation of an AAMV, in Take-off Phase. *J. Braz. Soc. Mech. Sci. Eng.* **2015**, *37*, 987–999. [[CrossRef](#)]
15. Amiri, M.M.; Dakhrabadi, M.T.; Seif, M.S. Formulation of a Nonlinear Mathematical Model to Simulate Accelerations of an AAMV in Take-off and Landing Phases. *Ships Offshore Struct.* **2014**, *11*, 198–212. [[CrossRef](#)]
16. Song, Y.; Du, X.; Jiang, Y.; Hu, Y. Numerical Investigation on the Resistance Characteristics and Motion Characteristics of the Ultra-High-Speed Aerodynamically Alleviated Marine Vehicle in Regular Head Waves. *Ocean Eng.* **2023**, *289*, 116284. [[CrossRef](#)]
17. Aliffrananda, M.H.N.; Sulistyono, A.; Hermawan, Y.A.; Zubaydi, A. Numerical Analysis of Floatplane Porpoising Instability in Calm Water During Takeoff. *Int. J. Technol.* **2022**, *13*, 190–201. [[CrossRef](#)]
18. Mansoori, M.; Fernandes, A.C. The Interceptor Hydrodynamic Analysis for Controlling the Porpoising Instability in High Speed Crafts. *Appl. Ocean Res.* **2016**, *57*, 40–51. [[CrossRef](#)]
19. Ding, R.; Zhang, H.; Xu, D.; Liu, C.; Shi, Q.; Liu, J.; Zou, W.; Wu, Y. Experimental and Numerical Study on Motion Instability of Modular Floating Structures. *Nonlinear Dyn.* **2022**, *111*, 6239–6259. [[CrossRef](#)]
20. Sukas, O.F.; Kinaci, O.K.; Cakici, F.; Gokce, M.K. Hydrodynamic Assessment of Planing Hulls Using Overset Grids. *Appl. Ocean Res.* **2017**, *65*, 35–46. [[CrossRef](#)]
21. De Luca, F.; Mancini, S.; Miranda, S.; Pensa, C. An Extended Verification and Validation Study of CFD Simulations for Planing Hulls. *J. Sh. Res.* **2016**, *60*, 101–118. [[CrossRef](#)]
22. Ding, J.; Jiang, J. Tunnel Flow of a Planing Trimaran and Effects on Resistance. *Ocean Eng.* **2021**, *237*, 109458. [[CrossRef](#)]
23. Roshan, F.; Dashtimanesh, A.; Bilandi, R.N. Hydrodynamic Characteristics of Tunneled Planing Hulls in Calm Water. *Brodogradnja* **2020**, *71*, 19–38. [[CrossRef](#)]
24. Su, G.; Shen, H.; Su, Y. Numerical Prediction of Hydrodynamic Performance of Planing Trimaran with a Wave-Piercing Bow. *J. Mar. Sci. Eng.* **2020**, *8*, 897. [[CrossRef](#)]

25. De Marco, A.; Mancini, S.; Miranda, S.; Scognamiglio, R.; Vitiello, L. Experimental and Numerical Hydrodynamic Analysis of a Stepped Planing Hull. *Appl. Ocean Res.* **2017**, *64*, 135–154. [[CrossRef](#)]
26. Trimulyono, A.; Luqman, M.; Chairizal, H.; Syaiful, A.; Putra, T.; Tuswan, A.T.; Wibawa, A.; Santosa, B. Analysis of the Double Steps Position Effect on Planing Hull Performances. *Brodogr. Int. J. Nav. Archit. Ocean Eng. Res. Dev.* **2023**, *74*, 41–72. [[CrossRef](#)]
27. Samuel, S.; Mursid, O.; Yulianti, S.; Kiryanto; Iqbal, M. Evaluation of interceptor design to reduce drag on planing hull. *Brodogr. Int. J. Nav. Archit. Ocean Eng. Res. Dev.* **2022**, *73*, 93–110. [[CrossRef](#)]
28. Kim, Y.; Kim, K.H. Numerical Stability of Rankine Panel Method for Steady Ship Waves. *Ships Offshore Struct.* **2007**, *2*, 299–306. [[CrossRef](#)]
29. Pols, A.; Gubesch, E.; Abdussamie, N.; Penesis, I.; Chin, C. Mooring Analysis of a Floating OWC Wave Energy Converter. *J. Mar. Sci. Eng.* **2021**, *9*, 228. [[CrossRef](#)]
30. Bonci, M.; De Jong, P.; Van Walree, F.; Renilson, M.R.; Huijismans, R.H.M. The Steering and Course Keeping Qualities of High-Speed Craft and the Inception of Dynamic Instabilities in the Following Sea. *Ocean Eng.* **2019**, *194*, 106636. [[CrossRef](#)]
31. Uharek, S.; Cura-Hochbaum, A. The Influence of Inertial Effects on the Mean Forces and Moments on a Ship Sailing in Oblique Waves Part B: Numerical Prediction Using a RANS Code. *Ocean Eng.* **2018**, *165*, 264–276. [[CrossRef](#)]
32. Hashimoto, H.; Yoneda, S.; Omura, T.; Umeda, N.; Matsuda, A.; Stern, F.; Tahara, Y. CFD Prediction of Wave-Induced Forces on Ships Running in Irregular Stern Quartering Seas. *Ocean Eng.* **2019**, *188*, 106277. [[CrossRef](#)]
33. Du, X.; Ali, N.; Zhang, L. Numerical Simulations for Predicting Wave Force Effects on Dynamic and Motion Characteristics of Blended Winged-Body Underwater Glider. *Ocean Eng.* **2021**, *235*, 109312. [[CrossRef](#)]
34. Faltinsen, O. *Sea Loads on Ships and Offshore Structures*; Cambridge University Press: Cambridge, UK, 1993.
35. Fossen, T.I. *Handbook of Marine Craft Hydrodynamics and Motion Control*; John Wiley & Sons: Hoboken, NJ, USA, 2011. [[CrossRef](#)]
36. John, F. On the Motion of Floating Bodies. I. *Commun. Pure Appl. Math.* **1949**, *2*, 13–57. [[CrossRef](#)]
37. ANSYS Inc. Aqwa Theory Manual. *Ansys* **2015**, 15317, 174.
38. ITTC Resistance Committee ITTC. Uncertainty Analysis in CFD, Validation and Validation Methodology and Procedures, 7.5–03-01–01. ITTC—Recommended Procedures and Guidelines Register. 2017; pp. 1–13. Available online: <https://www.itc.info/media/8153/75-03-01-01.pdf> (accessed on 1 July 2024).

**Disclaimer/Publisher’s Note:** The statements, opinions and data contained in all publications are solely those of the individual author(s) and contributor(s) and not of MDPI and/or the editor(s). MDPI and/or the editor(s) disclaim responsibility for any injury to people or property resulting from any ideas, methods, instructions or products referred to in the content.